The Madden–Julian Oscillation Simulated in the NCEP Climate Forecast System Model: The Importance of Stratiform Heating

KYONG-HWAN SEO

Department of Atmospheric Sciences, Pusan National University, Busan, South Korea

WANQIU WANG

Climate Prediction Center, NOAA/NWS/NCEP, Camp Springs, Maryland

(Manuscript received 15 December 2008, in final form 30 March 2010)

ABSTRACT

This study investigates the capability for simulating the Madden–Julian oscillation (MJO) in a series of atmosphere–ocean coupled and uncoupled simulations using NCEP operational general circulation models. The effect of air–sea coupling on the MJO is examined by comparing long-term simulations from the coupled Climate Forecast System (CFS T62) and the atmospheric Global Forecast System (GFS T62) models. Another coupled simulation with a higher horizontal resolution model (CFS T126) is performed to investigate the impact of model horizontal resolution. Furthermore, to examine the impact on a deep convection scheme, an additional coupled T126 run (CFS T126RAS) is conducted with the relaxed Arakawa–Schubert (RAS) scheme. The most important factors for the proper simulation of the MJO are investigated from these runs.

The empirical orthogonal function, lagged regression, and spectral analyses indicated that the interactive air–sea coupling greatly improved the coherence between convection, circulation, and other surface fields on the intraseasonal time scale. A higher horizontal resolution run (CFS T126) did not show significant improvements in the intensity and structure. However, GFS T62, CFS T62, and CFS T126 all yielded the 30–60-day variances that were not statistically distinguishable from the background red noise spectrum. Their eastward propagation was stalled over the Maritime Continent and far western Pacific. In contrast to the model simulations using the simplified Arakawa–Schubert (SAS) cumulus scheme, CFS T126RAS produced statistically significant spectral peaks in the MJO frequency band, and greatly improved the strength of the MJO convection and circulation. Most importantly, the ability of MJO convection signal to penetrate into the Maritime Continent and western Pacific was demonstrated. In this simulation, an early-stage shallow heating and moistening preconditioned the atmosphere for subsequent intense MJO convection and a top-heavy vertical heating profile was formed by stratiform heating in the upper and middle troposphere, working to increase temperature anomalies and hence eddy available potential energy that sustains the MJO. The stratiform heating arose from convective detrainment of moisture to the environment and stratiform anvil clouds. Therefore, the following factors were analyzed to be most important for the proper simulation of the MJO rather than the correct simulations of basic-state precipitation, sea surface temperature, intertropical convergence zone, vertical zonal wind shear, and lower-level zonal winds: 1) an elevated vertical heating structure (by stratiform heating), 2) a moisture–stratiform instability process (a positive feedback process between moisture and convective–stratiform clouds), and 3) the low-level moisture convergence to the east of MJO convection (through the appropriate moisture and convective–stratiform cloud processes–circulation interactions). The improved MJO simulation did improve the global circulation response to the tropical heating and may extend the predictability of weather and climate over Asia and North America.

Corresponding author address: Dr. Kyong-Hwan Seo, Department of Atmospheric Sciences, Pusan National University, Busan, South Korea.
E-mail: khseo@pusan.ac.kr

DOI: 10.1175/2010JCLI2983.1

1. Introduction

The Madden–Julian oscillation (MJO) has been considered a result of internal atmospheric dynamics involving the interaction between tropical convection and large-scale circulation. While some of the major MJO characteristics can indeed be simulated by atmospheric models with prescribed sea surface temperatures (SST), the results from many studies suggest the importance of air–sea interaction in the MJO dynamics. Observational and modeling diagnoses have shown coherent variations in surface heat fluxes, SST, and convection associated with the MJO (e.g., Krishnamurti et al. 1988; Slingo et al. 1996; Zhang 1996; Woolnough et al. 2000), indicating that interactive air–sea coupling needs to be included in numerical models to obtain a reasonable representation of the MJO.

In reality, however, improvements in the general circulation model (GCM) for the MJO simulation and forecast by this inclusion are considerably limited and dependent upon a GCM (Flatau et al. 1997; Waliser et al. 1999; Hendon 2000; Inness and Slingo 2003; Lin et al. 2006; Seo et al. 2005, 2007, 2009; Fu et al. 2008; Kim et al. 2009b). For example, if a coupled model fails to capture the observed convection–heat flux relationships because of any model deficiencies such as the generation of erroneous mean surface wind fields and SST (Hendon 2000; Inness and Slingo 2003), the simulated MJO may not be satisfactorily improved (Sperber et al. 2005). The recent study of Lin et al. (2006) demonstrates that only two models out of 14 coupled GCMs participating in the Intergovernmental Panel on Climate Change (IPCC) Fourth Assessment Report (AR4) are able to simulate the MJO variance and pronounced 30–60-day period spectral peak comparable to the observations.

The deficiencies apparent in MJO simulation can be attributed to many factors not limited to the previously mentioned air–sea coupling. The applied deep convection scheme is seemingly one of the most sensitive elements. A few studies have shown that the addition of moisture triggers to cumulus convection schemes significantly improves the MJO simulation (e.g., Tokioka et al. 1988; Wang and Schlesinger 1999). The MJO evaluation in IPCC AR4 models by Lin et al. (2006) confirmed that GCMs that employed convective triggers or triggers linked to moisture convergence can simulate the MJO. Recently, much progress in understanding the moist process associated with the development and maintenance has been made by observational data (Lin et al. 2004; Benedict and Randall 2007) and modeling studies (Zhang and Mu 2005; Boyle et al. 2008; Zhu et al. 2009; Fu and Wang 2009). This indicates that, prior to the onset of deep convection, shallow cumulus and cumulus congestus clouds transport heat and moisture upward, preconditioning the atmosphere for ensuing intense MJO convection through destabilization. Stratiform precipitation process also plays a critical role in the maintenance of the MJO by elevating a vertical heating profile and generating eddy available potential energy (Lin et al. 2004; Fu and Wang 2009). It is estimated from the Tropical Rainfall Measuring Mission (TRMM) precipitation radar (PR) data that stratiform precipitation fraction is ~40% of the total rain amount across the global tropics (Schumacher and Houze 2003). Recently, Fu and Wang (2009) show that the ECHAM4 model can simulate the robust MJO when the model produces a significant fraction (>30%) of stratiform precipitation. The convective detrainment of moisture to the stratiform clouds plays a key role in sustaining the MJO by inducing the characteristic heating profile associated with stratiform component and leading to a top-heavy heating profile. Also, it is shown that the detrainment from the convective updrafts moistens the large-scale environment and induces the further development of the deep convective plumes. This moisture–stratiform instability mechanism applied to originally the convectively coupled equatorial waves (e.g., Mapes 2000; Kuang 2008) is considered one of the most important processes for the enhanced and reasonable simulation of the MJO. This process will be investigated in this study.

Another factor is model resolutions. A higher horizontal resolution is shown to enable the MJO to move across the Maritime Continent as in Inness and Slingo (2006), and an increased vertical spacing might play a role to some degree (Inness et al. 2001). Time mean basic-state circulation and wind shear over the tropics are also believed to be important controlling elements for the correct MJO simulation (e.g., Inness et al. 2003). For example, a low-level easterly wind bias inhibits the MJO from propagating to the east (e.g., Flatau et al. 1997; Inness and Slingo 2003), while a vertical easterly zonal wind shear tends to favor eastward-moving waves (Zhang and Geller 1994). Furthermore, the appropriate representation of mean state SST is considered a prerequisite for the improved MJO simulation since a cold SST bias adversely affects convective activity (e.g., Inness and Slingo 2003). As noted above, moisture convergence plays a crucial role in developing and sustaining the MJO. The ultimate key to the MJO simulation is dependent upon whether models accurately simulate the persistent interaction of lower-level circulation waves and deep convection, as revealed by many previous observational and modeling studies (e.g., Maloney and Hartmann 1998; Waliser et al. 1999; Matthews 2000; Seo and Kim 2003; Lin et al. 2006).

Recently, an atmosphere–ocean coupled Climate Forecast System (CFS) model with the horizontal resolution

of T62 was developed by the National Centers for Environmental Prediction (NCEP) and has been running in an operational format since 2004. Several coupled simulations using this version have been performed along with an atmosphere-alone Atmospheric Model Intercomparison Project (AMIP) simulation. Additionally, the higher-resolution CFS model adopting a T126 grid system was run to produce long-term integrated data. Furthermore, the CFS T126 model run that employs a different deep convection scheme has been also conducted to test the impact of the cumulus scheme on various climate oscillations and teleconnections. All these simulations have made it possible to evaluate the effects of air–sea interaction, model resolution, and deep convection scheme on the MJO. In addition, comparison of these runs provides an opportunity to investigate key factors for the proper MJO simulation.

In this study, we use a series of atmosphere-only and coupled model runs that employ different settings of horizontal resolution and a deep convection scheme to investigate the capability of the MJO simulation and deduce the important factors. The global response to the simulated MJO is examined. The following questions are addressed:

1) How well do the NCEP coupled models with a higher model resolution and a deep convection parameterization scheme simulate the basic characteristics and dynamics of the MJO?
2) Is a proper simulation of atmospheric and oceanic basic states a prerequisite for the realistic simulation of the MJO?
3) What factors are most important associated with moist convection?
4) Does the improved MJO simulation lead to the enhanced global circulation response?

The fourth question is especially important in that the final applications for the skillful prediction of weather and climate require the improved simulation of tropical forcing.

2. The simulations and data

a. The models

The NCEP coupled model (CFS) consists of the NCEP Global Forecast System (GFS) model and the Geophysical Fluid Dynamics Laboratory (GFDL) Modular Ocean Model version 3 (MOM3; Pacanowski and Griffies 1998). The atmospheric component of the coupled model is the 2003 version of the GFS model with a spectral truncation of T62 waves in the horizontal and a finite differencing in the vertical with 64 sigma layers. The GFS with a higher spatial resolution of T126 is also utilized. The MOM3 domain in CFS is quasi-global extending from 74°S to 64°N. The meridional resolution is $\frac{1}{3}$° between 10°S and 10°N, gradually increasing through the tropics until becoming fixed at 1° poleward of 30°S and 30°N, and the zonal resolution is 1°. There are 40 layers in the vertical with 27 layers in the upper 400 m. The atmospheric and oceanic components are coupled without any flux adjustment. Sea ice extent is prescribed from the observed climatology. More detailed descriptions of the CFS model can be found in Wang et al. (2005) and Saha et al. (2006).

b. The simulations and observations

The tropical instraseasonal variability, including the MJO, is diagnosed based on an atmosphere-alone AMIP-type simulation and a coupled long-term simulation. The AMIP simulation is performed using the GFS model with T62 resolution (GFS T62) that is forced with the observed monthly mean SST from 1982 to 2002. The prescribed SSTs are taken from the weekly analysis of Reynolds et al. (2002). Among several coupled simulations that are conducted with the CFS model, two runs with a resolution of T62 and T126 are executed to test the sensitivity to the horizontal resolution (CFS T62 and CFS T126, respectively). This simulation is initialized from the observed analyses of 1 January 2002 and run for 21 yr. The initial condition for the atmosphere is taken from the NCEP–Department of Energy (DOE) reanalysis-2 (R2; Kanamitsu et al. 2002) and the initial condition for the ocean was driven from an NCEP global ocean data assimilation system (GODAS; e.g., Seo and Xue 2005). The AMIP and coupled simulations are based on the simplified Arakawa–Schubert (SAS) cumulus parameterization scheme (Pan and Wu 1995). Therefore an additional coupled T126 run is performed with the relaxed Arakawa–Schubert (RAS) scheme (Moorthi and Suarez 1992) to examine the impact of the deep convection scheme. This simulation is called CFS T126RAS and is run from 2002 to 2016. The SAS scheme used is the modified scheme of Pan and Wu (1995) to the original Arakawa–Schubert scheme (Arakawa and Schubert 1974) as simplified by Grell (1993). It includes a saturated downdraft parameterization. RAS (Moorthi and Suarez 1999) implemented in this study is based on the modifications of the original scheme of Moorthi and Suarez (1992). The major modifications include the consideration of downdraft, evaporation of precipitation, and some cloud model improvements. Each cloud type is considered to relax to a quasi-equilibrium state. One of main differences is that SAS only considers one simple deepest cloud and detrainment at the cloud top, but RAS considers a spectrum of cloud types and allows the convective detrainment at various levels. This difference results in the different detrainment of water vapor from convective

cloud in the middle and upper troposphere and vertical heating profiles, which affects the development and propagation of the MJO. A brief description of these convection schemes can be found in Das et al. (2002).

The observational data used in this study comprise R2, the Climate Prediction Center Merged Analysis of Precipitation (CMAP; Xie and Arkin 1997), and daily Advanced Very High Resolution Radiometer (AVHRR) outgoing longwave radiation (OLR; Liebmann and Smith 1996) from 1982 to 2002. CMAP precipitation is interpolated from pentad analyses to daily data. Calculations for the MJO are based on 20–100-day bandpass-filtered anomalies using a Lanczos filter (Duchon 1979).

3. Methods

First, to evaluate the capability of simulating the MJO along the tropics, the spectral power spectra are calculated using OLR anomaly data and this is compared to the upper 95% confidence limit of background noise. The background noise is computed as the red spectrum using a lag-1 autocorrelation. Accordingly, the spectral values greater than this upper limit of red noise are considered statistically significant signals associated with the MJO.

The MJO is the combined system of convection and large-scale circulation. So to identify the MJO's dominant spatial structure, empirical orthogonal functions (EOFs) of the combined fields of 10°S–10°N averaged 850-hPa zonal wind (u850), 200-hPa zonal wind (u200), and OLR are calculated (Wheeler and Hendon 2004; Seo et al. 2009; Kim et al. 2009a). Prior to inputting into the EOF analysis, each variable is normalized by its global-averaged variance such that each variable retains the same amount of weighting in the calculation of the covariance of the combined fields.

4. Results

a. The MJO

One of the pronounced features associated with the MJO is the appearance of the spectral peaks in a broad band of ~(30–80)-day periods. To determine whether the model simulations produce the spectral peaks, we first examine the power spectra in convection anomalies in the observation and the four simulations. Figure 1 shows the power spectra of the OLR anomalies averaged over the tropical Indian Ocean (left panels) and the tropical western Pacific (right panels), where the MJO convection is developed and strengthened. In the plot, the area below the curve is proportional to the explained variance. The observed spectrum (Fig. 1a) measured by the smoothed periodogram (thick line) illustrates that a higher power exists in the intraseasonal band of 30–80-day periods with a center around 40–55 days. These spectral peaks stand out with respect to the upper 95% confidence limit of background noise (dotted line). However, GFS T62 and CFS T62 (Figs. 1b,c, respectively) do not show any significant spectral peaks associated with the MJO. On the contrary, CFS T62 produces a spectrum that is too fat for periods greater than 1 yr. It seems that CFS T126 (Fig. 1d) displays a somewhat improved power spectrum compared to CFS T62, but the spectral power in the 30–80-day band is lower than the red background noise. In contrast to the model simulations using the SAS cumulus scheme, CFS T126RAS (Fig. 1e) produces statistically significant spectral peaks in the MJO band. Several peaks exist in the 30–80-day band. Overall, it shows greater convective activity along the tropics over all spectral range, consistent with the previous findings and experience. All these features in the observation and models appear for the western Pacific region also. That is, the statistically significant intraseasonal signals are existent only for the observation (Fig. 1f) and CFS T126RAS (Fig. 1j), but other model runs using the SAS scheme do not produce statistically significant peaks (Figs. 1g–i). Thus, the only model that simulates the statistically significant spectral peak in the MJO band is the atmosphere–ocean coupled model running with a higher horizontal resolution (T126) and adopting the RAS deep convection scheme.

Figure 2 shows the two leading EOF modes of tropical convection–circulation fields. Since their principal components (PCs) are strongly correlated with a 7–10-day lag (Fig. 3), in combination they describe the large-scale, eastward-propagating MJO signal. The first EOF (EOF1) of the observation (Fig. 2a) is characterized by a strong convective heat source over the Maritime Continent and the western Pacific (100°–160°E), and a consistent convergent flow in the lower troposphere and a divergent flow in the upper troposphere, reminiscent of a Gill-type response. In the second EOF (EOF2; Fig. 2b), enhanced convection is located over the Indian Ocean from 60° to 100°E. By contrast, in the GFS T62 run, the EOF1 peak location (Fig. 2c) appears at 150°E, rather than over the Maritime Continent shown in the observation, and the western boundary of EOF1 convective heating is seen over the eastern Indian Ocean, which is situated farther east compared with the observation. Although the structure of EOF2 (Fig. 2d) over the Indian Ocean appears to be similar to the observation, it fails to generate suppressed convection over the western Pacific.

Meanwhile, slight improvements appears in CFS T62 (Figs. 2e,f) compared to GFS T62 appears including the zonal variations of the upper- and lower-level winds for

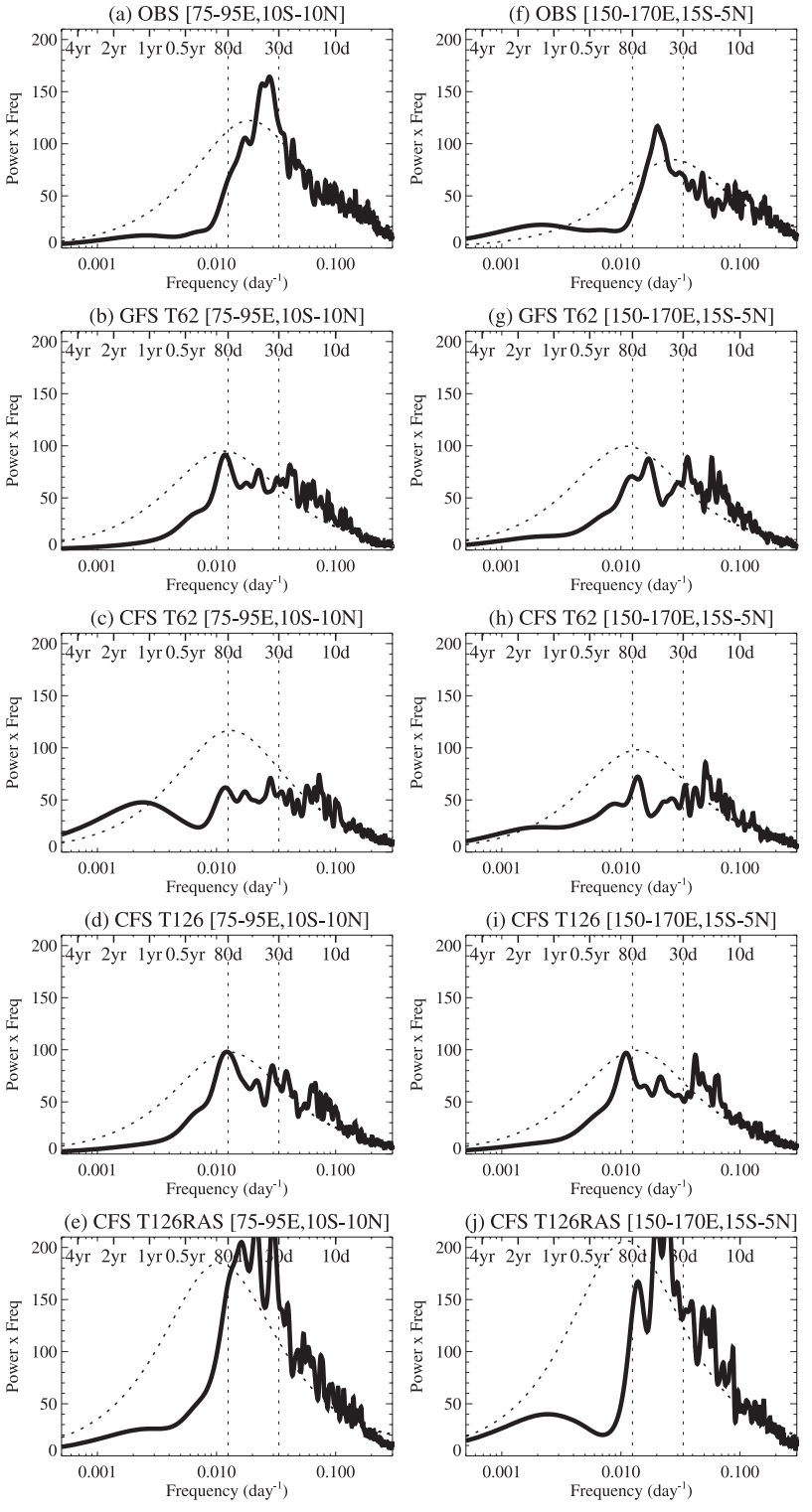

FIG. 1. Power spectra of OLR anomalies averaged over (left) the tropical Indian Ocean area (10°S–10°N, 75°–95°E) and (right) the western Pacific region (15°S–5°N, 150°–170°E) for (a),(f) observations, (b),(g) GFS T62, (c),(h) CFS T62, (d),(i)CFS T126, and (e),(j) CFS T126RAS. The thick lines represent the smoothed power. The dashed curve is the upper 95% confidence limit of the red noise spectrum calculated from a lag-1 autocorrelation. The smoothed spectra are calculated from the Parzen window having an effective bandwidth of 2.5×10^{-3} cycles per day (cpd). For clarity, 30- and 80-day period lines are denoted by dotted vertical lines.

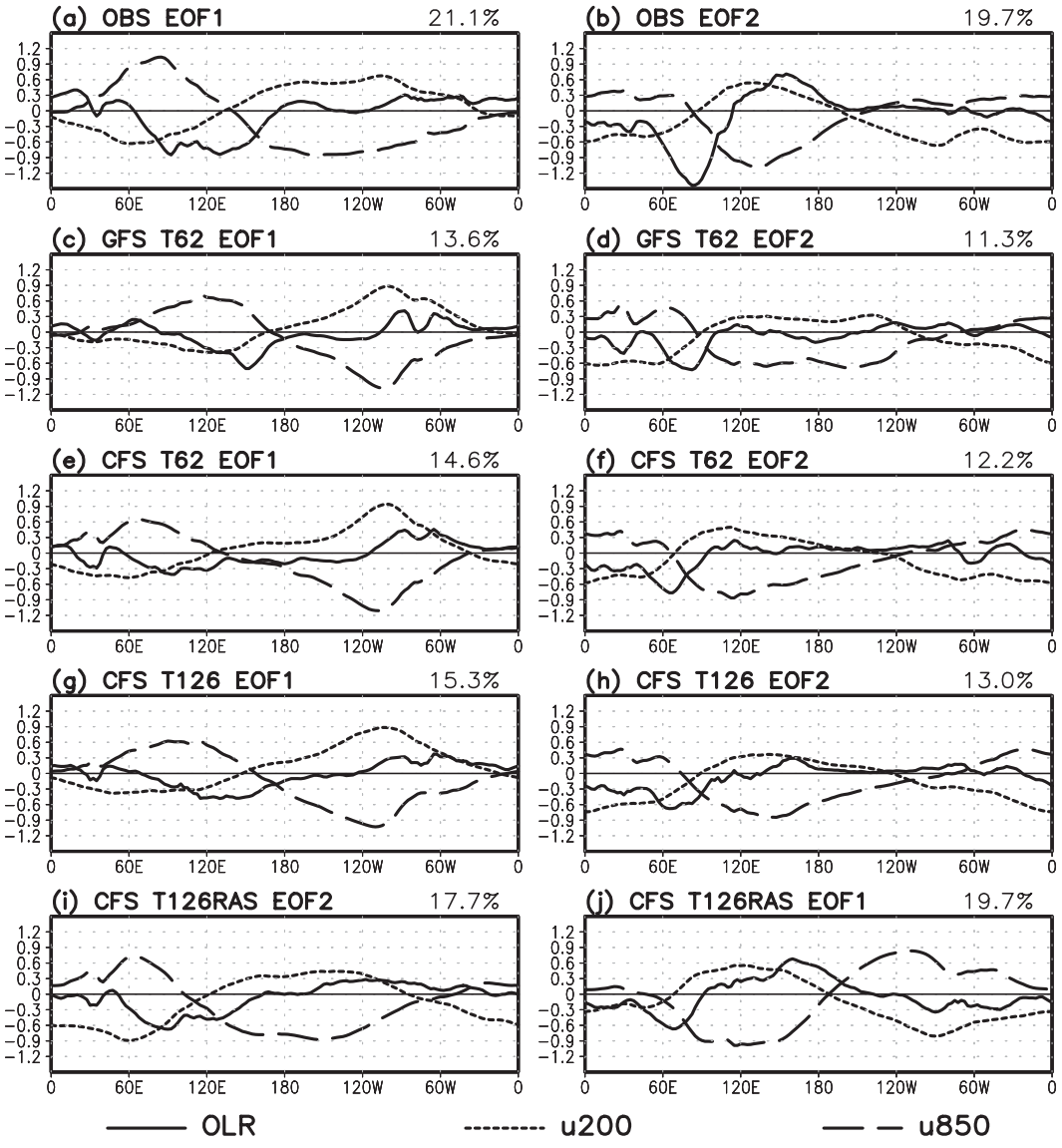

FIG. 2. Spatial structures of combined EOFs of 20–100-day filtered OLR, u850, and u200. EOF1 and EOF2 from (a),(b) observations; (c),(d) GFS T62, (e),(f) CFS T62; (g),(h) CFS T126; and (j),(i) CFS T126RAS. Note that EOF1 (EOF2) of CFS T126RAS is shown in right (left). OLR, u850, and u200 are plotted in solid, dashed, and dotted lines, respectively. The percentage value above each is the variance explained by each mode and scaled against the observations. All variables are normalized by the averaged value of global variance (9.06 W m^{-2} for OLR, 1.25 m s^{-1} for u850, and 3.51 m s^{-1} for u200).

both EOF1 and EOF2 and a slight increase in the variance explained by these two modes. The higher resolution CFS simulation (CFS T126; Figs. 2g,h) exhibits a similar spatial distribution to CFS T62. Note that the explained variance for each PC is presented in the figure and for the sake of a fair comparison of this variance among the model simulations, all values are adjusted against the total variance in the observations by multiplying the originally computed explained variance by a square root ratio between the total variances in the simulations and observations. Then, we can see that in GFS T62, CFS T62, and CFS T126, the explained variance is more than 28% weaker than the observation. However, the CFS T126RAS run (Figs. 2i,j) shows some improved results. In particular, the strength of the MJO convection and circulation is greatly enhanced for both EOF1 and EOF2. However, the center of the convection and circulation anomalies are shifted ~(20°–40°) to the east and the zonal scale of the enhanced convection over the Indian Ocean in EOF2 is too broad. All the

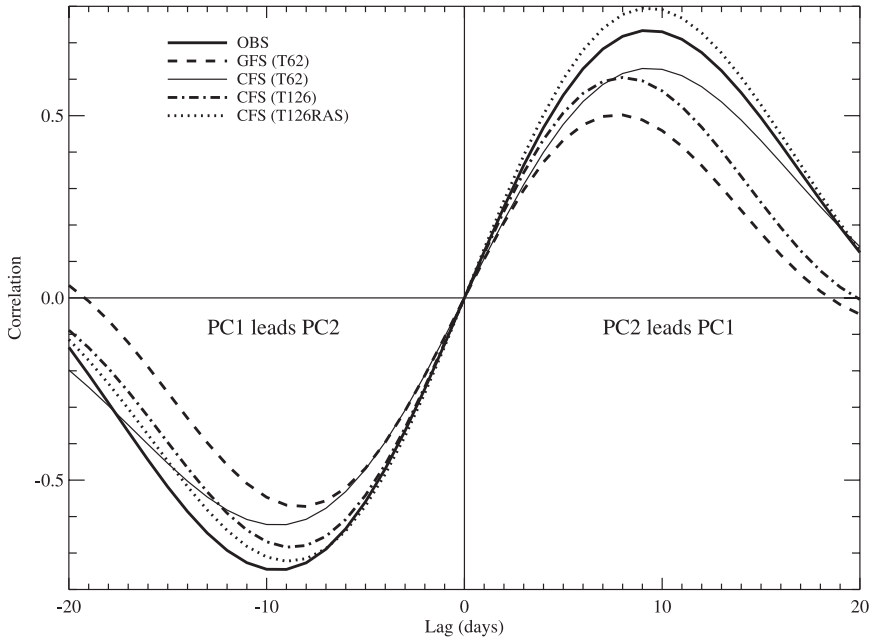

FIG. 3. Lag correlation between the two PCs. A positive lag means that PC2 leads PC1 except for CFS T126RAS where PC1 leads PC2.

simulations show some systematic limitations in simulating the MJO. For example, the models produce an excessively strong signal over the eastern Pacific for EOF1 and experience difficulties in producing suppressed convection over the western Pacific.

The plot of lag correlation between two PCs is shown in Fig. 3, where positive lag means that EOF2 leads EOF1, but for CFS T126RAS, positive lag means that EOF1 leads EOF2. Since two EOFs correspond to active convection in the Indian Ocean and in the Maritime Continents–western Pacific areas, the lag where correlation reaches maximum values approximates the propagation time from the Indian Ocean to the western Pacific or a quarter of the oscillation period. The figure indicates that such a propagation time is about 9 days in both the observation and CFS T126RAS, but 7–8 days in GFS T62 and CFS T126. Aside from the similar propagation speed that appeared in CFS T126 RAS, its correlation value is larger than the observation at the positive lag, indicating the generation of stronger MJO signal. In contrast, other model runs produce smaller correlations compared to the observation and thus a less robust MJO signal.

From this EOF analysis, it is difficult to ascertain whether air–sea interaction, cumulus parameterization scheme, and the increased horizontal resolution induce the overall improvements or changes. Instead, it is very helpful to determine the propagation characteristics along the equator in the MJO-related dynamic and thermodynamic fields. For this, lag correlations are calculated between the PC time series of the combined EOF and the associated individual fields (e.g., u850, precipitation rate, OLR, surface latent heat flux, downward solar radiation flux, surface temperature, and 1000-hP moisture convergence). Figure 4 shows the lag correlations between the PC time series of EOF2 (or PC2) and the individual fields. The lag correlation maps using PC2 facilitate the illustration of MJO propagation from the Indian Ocean, and similar results are obtained based on the lag correlation of these fields with the PC time series of EOF1 (or PC1). The observations indicate that the precipitation and OLR anomalies develop over the Indian Ocean, propagate across the Maritime Continent and western Pacific, and decay near the date line with decreased SST. As seen in the Fig. 2, 850-hPa zonal wind shows westerly anomalies to the west of the enhanced convection and easterly anomalies to the east. Since the annual mean surface zonal winds are weak westerlies over the MJO convection regions, enhanced evaporation (i.e., enhanced negative latent heat flux to the atmosphere) appears to the west of the convection and reduced evaporation (downward positive latent heat flux) to the east of the convection. In addition, the suppressed convection associated with the negative rainfall anomalies results in positive downward solar radiation at the surface from day −20 to 0. Both latent heat and solar radiation fluxes heat the surface, leading to the development of a warm SST anomaly. The surface heating precedes the enhanced convection by a quarter cycles [~(10–12 days)]

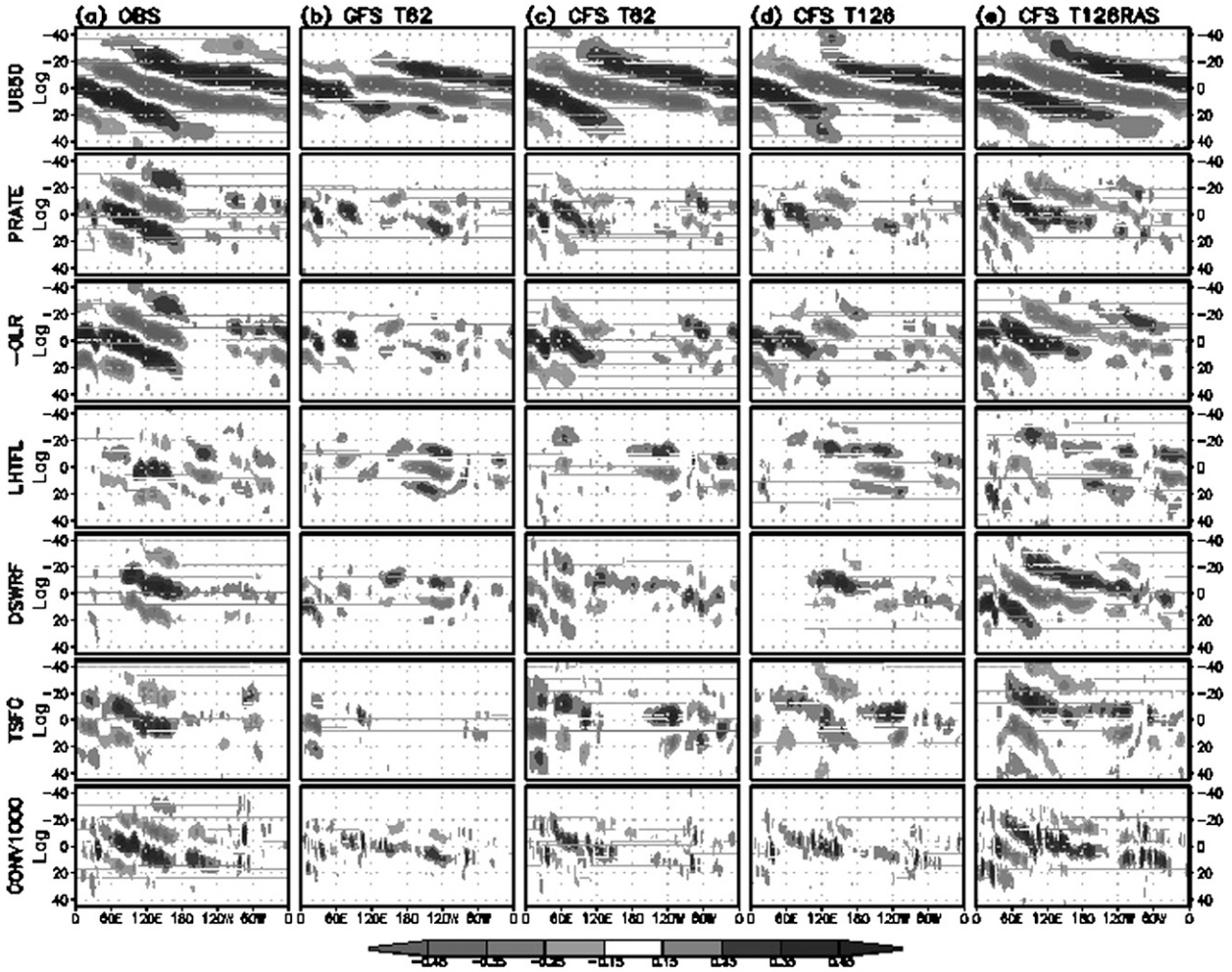

FIG. 4. Lag correlation coefficient between PC2 and (top to bottom) u850, precipitation rate, −OLR, downward latent heat flux, surface downward solar radiation flux, surface temperature, and 1000-hPa moisture convergence for (a) observations, (b) GFS T62, (c) CFS T62, (d) CFS T126, and (e) CFS T126RAS. The moisture convergence is defined as $-\mathbf{V}\cdot(\mathbf{V}q)$, where $\mathbf{V}$ is the velocity vector and q is the specific humidity. Only statistically significant regions at the 95% level are shaded.

and assists in the moisture convergence ahead of the enhanced convection. The surface moisture convergence leads the convection anomaly by 2–5 days. This characteristic is consistent with the frictional wave-conditional instability of the second kind (CISK) theory (e.g., Wang 1988; Salby et al. 1994; Seo and Kim 2003), which is the currently prevailing paradigm for the MJO's development and maintenance mechanisms.

GFS T62 produces less pronounced precipitation and OLR anomalies (Fig. 4b), whereas the lower-level zonal wind anomaly tends to propagate more realistically because of the use of the observed SST forcing. Meanwhile, compared to GFS T62, CFS T62 (Fig. 4c) shows a much stronger convection signal and greater spatial coherence between the convection and surface fluxes, and SST over the Indian Ocean. Several peculiar shortcomings are evident. First, the evolution of latent heat flux in the simulation in the western Pacific is not consistent with that in the observation because of the failure of the simulation of the seasonal mean surface zonal wind in the region (refer to Fig. 6). In addition, the propagation is evidently stalled at the Maritime Continent and western Pacific. However, the improved coherence between the circulation and heating fields, and the consistent evolution of SSTs over the Indian Ocean suggest that interactive air–sea coupling is important for the MJO simulation. The CFS T126 run (Fig. 4d) exhibits basically the same features as CFS T62 with the stalled propagation appearing over the Maritime Continent and western Pacific. This lack of coherent eastward propagation from the Indian Ocean to the Pacific has also been noticed in forecast data (Seo et al. 2005) and even a CFS T62 simulation with flux adjustment (Seo et al. 2007), and other model simulations (e.g., Slingo et al. 1996;

Inness and Slingo 2003; Sperber et al. 2005). Only the propagation speed of the MJO convection over the Indian Ocean in CFS T126 is slightly improved compared to the much slower propagation in CFS T62.

By contrast, CFS T126RAS exhibits much improved propagation characteristics (Fig. 4e). The MJO convection signal (shown as precipitation and OLR anomalies) is very vigorous and this tends to penetrate into the Maritime Continent and western Pacific. The propagation is slower over the Indian Ocean than the observation but it is faster over the western Pacific. The downward shortwave radiation flux and surface temperature also propagate with similar lead–lag relationships with the MJO convection. The surface moisture convergence signal is the strongest among the simulations and moves across the Maritime Continent region and reaches the central Pacific. The surface temperature and moisture convergence are all located to the east of the deep convection, implying that this model produces the surface frictional convergence process as seen in the observations.

b. *Factors for the MJO simulation*

Only CFS T126RAS has demonstrated a capability to simulate the correct MJO. Other AMIP and coupled runs utilizing the SAS cumulus scheme show significant problems. This section presents the important factors for successfully simulating the MJO.

1) AIR–SEA INTERACTION

Comparison of the uncoupled and fully coupled model long-term simulations illustrates that the air–sea coupling improves the coherence between convection and circulation and other surface fields (Fig. 4). Over the Indian Ocean, the related MJO dynamics (including convection–circulation feedback and surface processes for flux, temperature, and convergence) in the coupled simulations shows a great resemblance to the observations.

2) MODEL HORIZONTAL RESOLUTION

As presented in Inness and Slingo (2006), a higher horizontal resolution model may be required to resolve the Maritime Continent region and thus properly simulate the basic characteristics associated with the MJO. The current CFS model runs demonstrate that an increase in the resolution from T62 (which corresponds to ~209 km) to T126 (~105 km) does not help improve the MJO simulation; however, a higher model resolution than T126 remains to be tested.

3) BASIC-STATE VERTICAL EASTERLY WIND SHEAR

Zhang and Geller (1994) showed that vertical easterly shear favors eastward-propagating waves. Figure 5 shows the annual mean vertical easterly shear (u200 and u850) over the Maritime Continent and the western Pacific (120°–170°E, 7.5°S–7.5°N) for the observation and model simulations. The values are converted to positive ones. The CFS simulations produce the easterly wind shear from about -2 to -4 m s^{-1}, which is much weaker than the observed shear (-6.4 m s^{-1}). The vertical wind shear in CFS T126RAS is less than one-third that of the observation. Although GFS T62 produces the most similar magnitude to the observed, which is expected since it is forced with the observed SST, and hence the climatology of the large-scale circulation resembles the observation, the previous figures indicate that the MJO cannot be reproduced in this atmosphere-only model simulation. These results imply that the background vertical easterly wind shear does not play a major role in the MJO simulation.

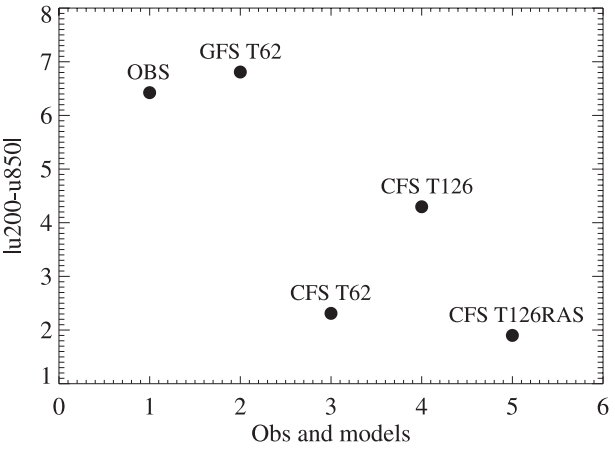

FIG. 5. Annual mean vertical zonal wind shear (u200 – u850) averaged over 10°S–10°N for observations and model runs. All values represent easterly shear but these are converted to positive values.

4) BASIC-STATE EASTERLY LOW-LEVEL ZONAL WIND ALONG THE TROPICS

Inness and Slingo (2003) and Flatau et al. (1997) suggest that the easterly bias acts as a barrier to the MJO's eastward propagation. Figure 6 shows the annual mean zonal wind at 850 hPa in the observation and simulations. Westerlies or weak easterlies are observed over the tropical Indian Ocean, Maritime Continent, and western Pacific (Fig. 6a), where the major development and propagation occur. By contrast, CFS T62 and CFS T126 exhibit significant easterly bias over those regions (Figs. 6b,c, respectively). Although the easterly bias in CFS T125RAS (Fig. 6d) is slightly decreased over the Maritime Continent and far western Pacific Ocean compared to the other CFS simulations, the westerlies remain weak over the

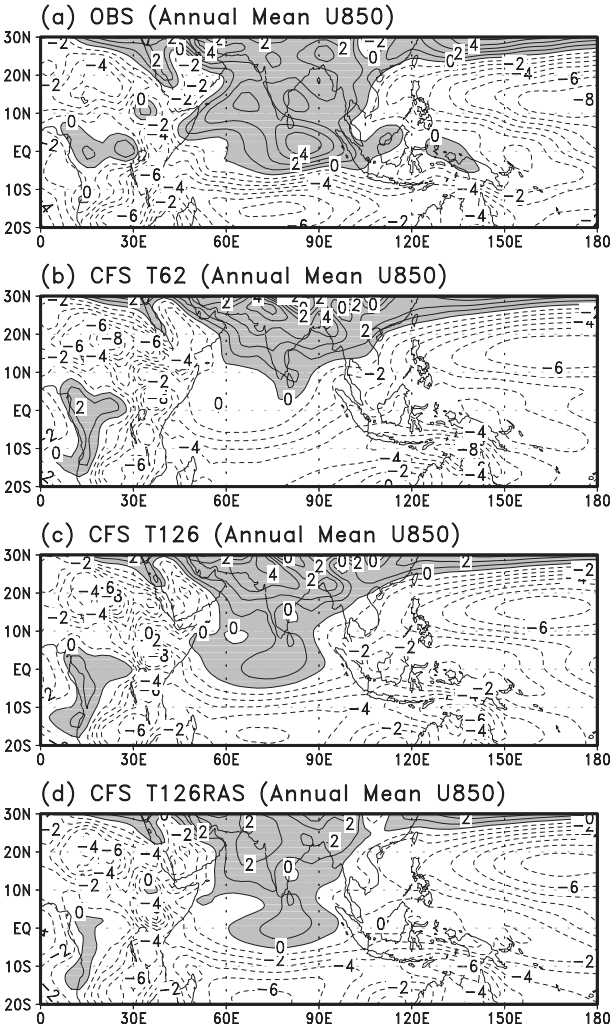

FIG. 6. Annual mean zonal wind (m s^{-1}) at 850 hPa for (a) observation, (b) CFS T62, (c) CFS T126, and (d) CFS T126RAS. The westerly regions are shaded.

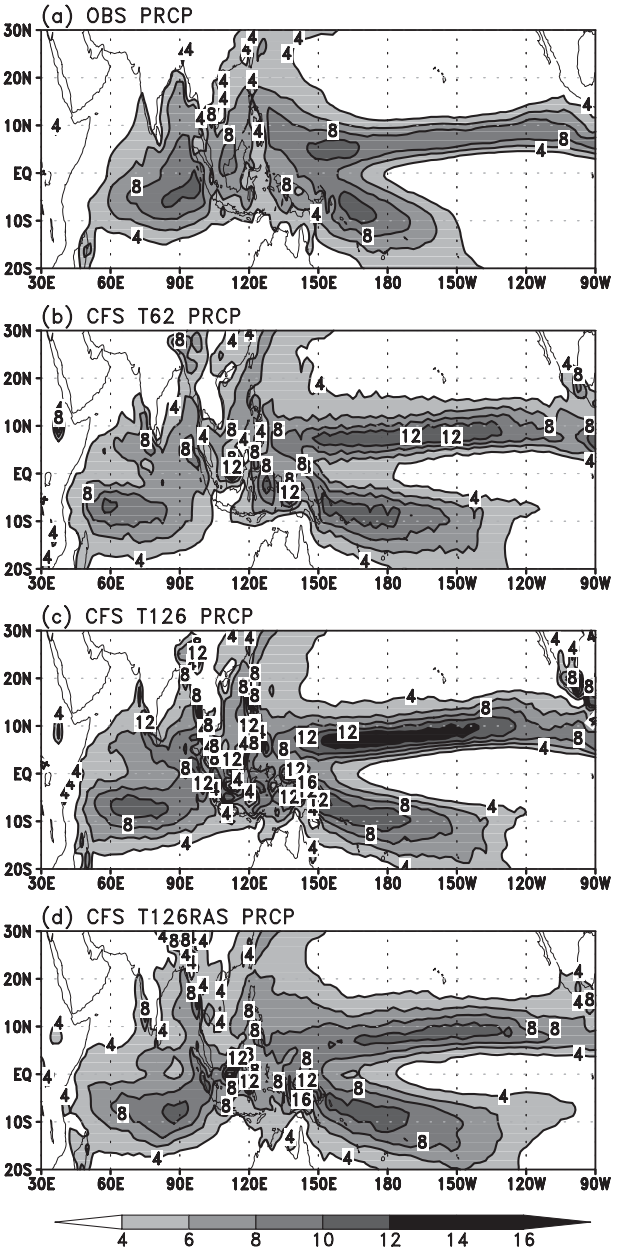

FIG. 7. Annual mean precipitation (mm) for (a) observation, (b) CFS T62, (c) CFS T126, and (d) CFS T126RAS.

central-eastern Indian Ocean and the easterly wind prevails over the Maritime Continent. These suggest that the basic-state easterly bias along the tropics may not be a major factor for the MJO simulation.

5) DOUBLE-ITCZ PROBLEM

Most of the coupled GCMs tend to produce a double ITCZ pattern for the basic-state precipitation. This bias is characterized by insufficient precipitation in the western Pacific and too excessive off-equator precipitation (Lin 2007). The negative precipitation bias over the equatorial western Pacific may suppress the intraseasonal variability, so the annual mean precipitation for the observation and CFS model runs is examined in Fig. 7. The figure shows that the all CFS model simulations have the double-ITCZ problem with the excessive precipitation along the Northern Hemisphere ITCZ and Southern Pacific convergence zone (SPCZ), together with the wrongly tilted SPCZ extending far to the east up to 120°W. Even if overall the insufficient precipitation bias along the equatorial western Pacific and the excessive precipitation bias in the off-equatorial regions in CFS T126RAS are smallest among the CFS simulations, the higher level of reproducibility of the basic-state precipitation does not seem to be a major factor in the case of the CFS model.

6) SST

A cold SST bias suppresses the development of the MJO convection. The SST bias, defined as model SST minus observed SST, is presented in Fig. 8 for the coupled simulations. A warm bias of ~(0.5°–1.0°C) appears over the western Indian Ocean, while a cold bias prevails over the eastern Indian Ocean and the western Pacific. The cold bias over the eastern Indian Ocean may be due to a stronger upwelling by the easterly bias in this region. The cold bias over the eastern Indian Ocean continues in CFS T126 (Fig. 8b). The tropical western Pacific cold bias disappears and a warm bias develops over the seas in the Maritime Continent, but these are insufficient for robust propagation over these regions. This implies that the removal of a cold SST bias cannot always guarantee the eastward propagation across the Maritime Continent to the date line as seen in the observations. CFS T126RAS shows that even if a cold bias exists over the tropical western Pacific, the MJO eastward propagation is greatly enhanced (Fig. 8c). The cold bias in the CFS models is part of the double-ITCZ problem (Lin 2007), which is signified by the significant SST bias in much of the tropical oceans and off equator in both the Northern and Southern Hemispheres. An independent CFS T62 simulation incorporating a surface flux correction (refer to Seo et al. 2007), which is not included in this study, also shows the stalled propagation near the Maritime Continent. In combination, these results suggest that in the absence of a huge SST bias, other factors may be more effective. Nonetheless, the possibility that the disappearance of a cold bias over the eastern Indian Ocean may strengthen the convective activity and help the oscillation propagate to the east cannot be ruled out. A more careful test needs to be conducted for the detailed evaluation of the SST effect.

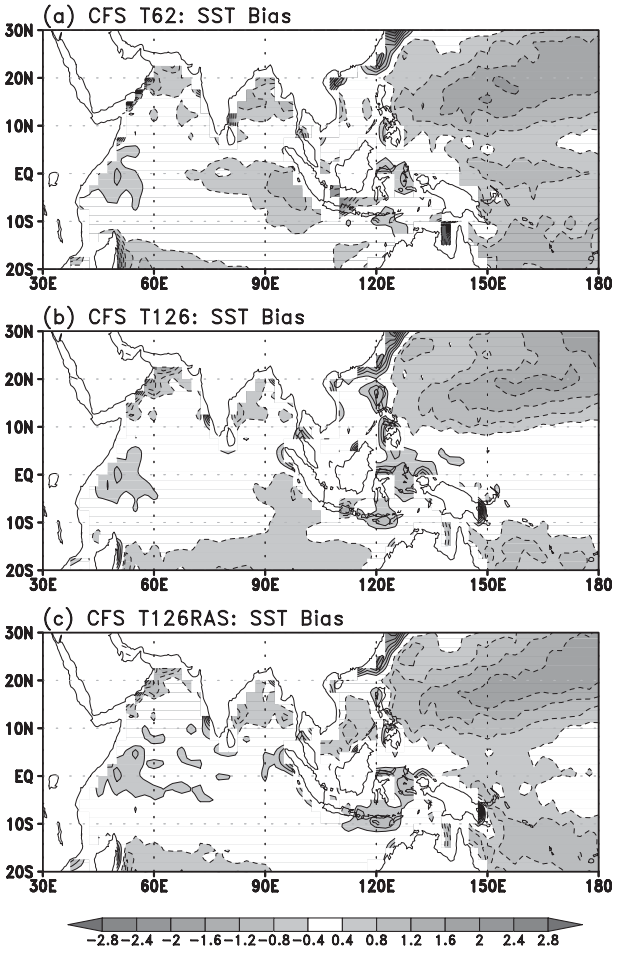

FIG. 8. Annual mean SST bias (°C) for (a) CFS T62, (b) CFS T126, and (c) CFS T126RAS.

7) MOIST PROCESS

The current analysis demonstrates that an apparent improvement when the NCEP coupled model utilizes the RAS scheme for cumulus parameterization. Then how to maintain the active convective activity along the tropics over the warm pools in this model should be examined. To do this, the vertical structures of the zonal and vertical winds, specific humidity, temperature, apparent heat source (Q1), and apparent moisture sink (Q2; Yanai et al. 1973) anomalies are constructed by regressing these variables onto MJO convection. Figures 9 and 10 show the vertical profiles of these regressions as a function of lag–lead day for the OLR anomalies averaged over 10°S–10°N and 110°–130°E for CFS T126RAS and CFS T126, respectively. For the observed profiles, refer to Benedict and Randall (2007, their Figs. 3 and 6).

We first examine the CFS T126RAS case in Fig. 10. It is seen that in zonal wind cross section (Fig. 10a), the transition from low-level easterly to westerly anomalies ~7 days before the convection maximum (day 0). The westerly zonal wind maximum appears ~(4–5) days after the peak convection, which is nearly consistent with the observations. Vertical velocity cross section shows maximum upward motion at the time of maximum convection activity, but also indicates weak upward motion in the lower troposphere approximately 10 days before the deep convection maximum (Fig. 10b). Along with this, the positive specific humidity anomalies are formed first in the surface about 10–15 days prior to the strong MJO convection and go upward to the lower troposphere beginning day −10, reaching 300 hPa at day −4 (Fig. 10c), thus, indicating some similarity to the observed profile. This shallow moistening preconditions the lower troposphere for the later development of deep convection. Maximum water vapor anomalies are formed

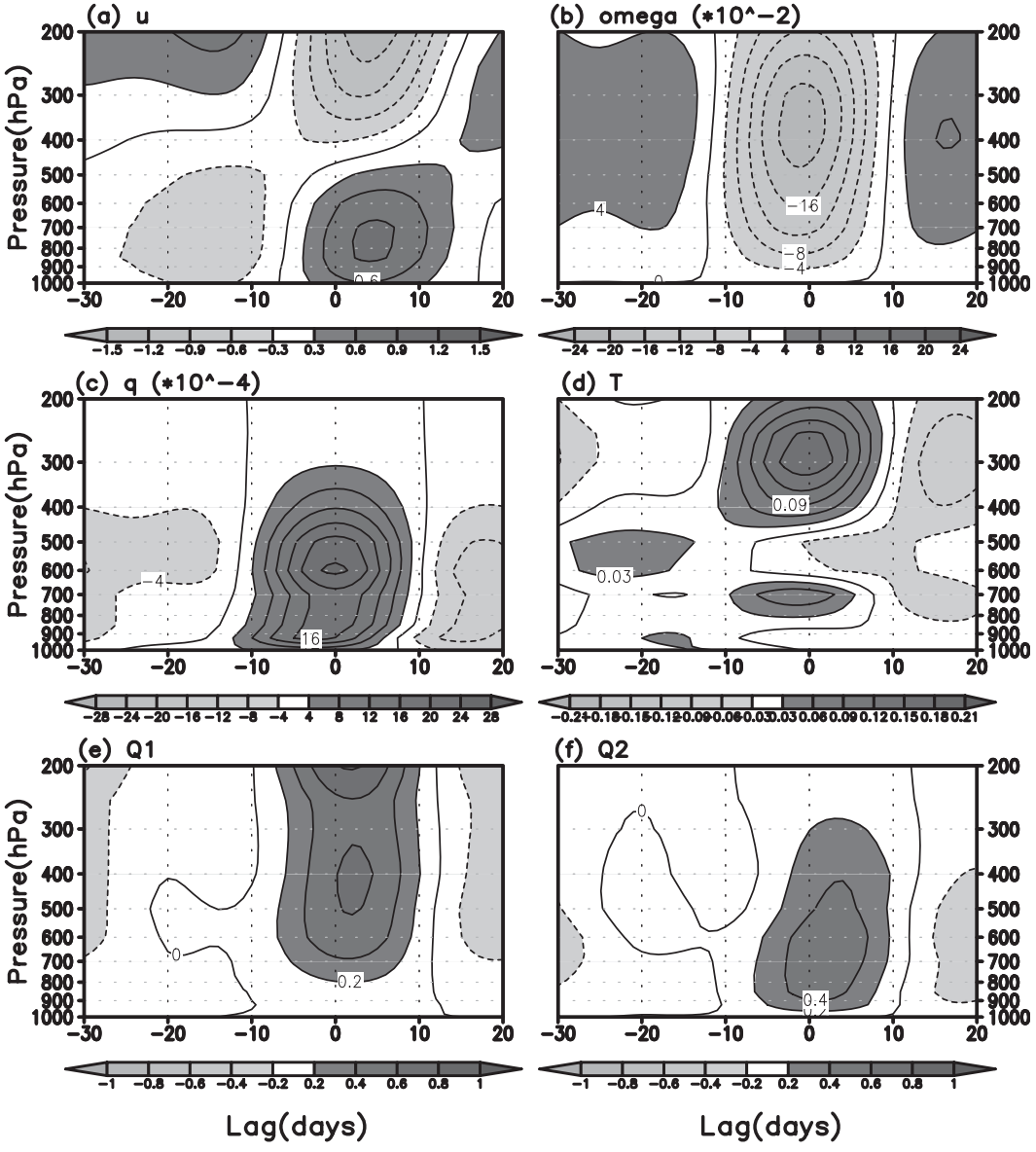

FIG. 9. Lag–height plots of (a) zonal wind (m s^{-1}), (b) pressure velocity (hPa $s^{-1} \times 100$), (c) specific humidity (g $kg^{-1} \times 10^4$), (d) temperature (K), (e) apparent heat source (Q1; K day^{-1}), and (f) apparent moisture sink (Q2; K day^{-1}), anomalies regressed onto OLR anomalies averaged over 10°S–10°N and 110°–130°E for CFS T126.

on day 0 between 500 and 600 hPa. Negative water vapor anomalies appear at the surface first at day +10.

The temperature profile (Fig. 10d) shows that the peak warm anomalies appear at the time of peak convection and are centered at 300 hPa (slightly higher than the observational peak of 350 hPa). Together with this, the negative temperature anomalies occur below 800 hPa. This structure is a signature of the effect of stratiform rainfall with the upper-level warm anomalies arising from condensational heating from stratiform clouds and the lower-level cool anomalies resulting from latent cooling in downdraft associated with the strong convection and the evaporation of stratiform rainfall (as will be seen later in Figs. 12 and 13; Benedict and Randall 2007). Another important feature arises in the lower troposphere between days −20 and −10, where weak warm anomalies develop. Along with the formation of moist air and weak upward motion, the warm anomalies signify the existence of shallow convection, which is associated with small cumulus and congestus clouds. The surface and low-level preconditioning is considered a key element for the ensuing amplification of MJO convection and its propagation to the east along the warm tropical ocean. The development of an early-stage shallow heating and

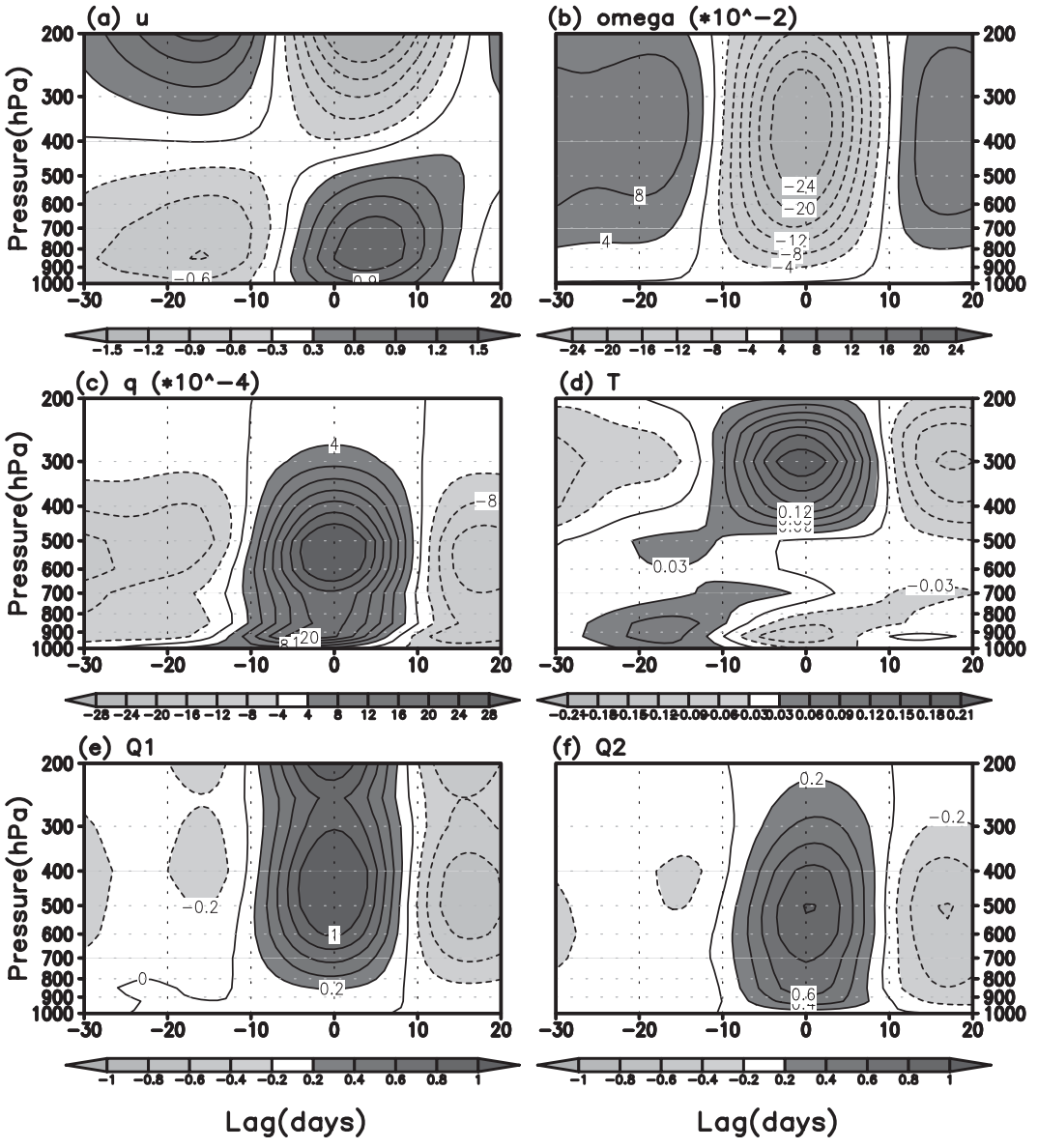

FIG. 10. As in Fig. 9, but for CFS T126RAS.

moistening and a peak-time top-heavy vertical heating profile is consistent with the observed properties. The apparent heat source (Q1; Fig. 10e) also shows this lower-level tendency between days −20 and −10, although not as strong as the temperature anomalies due to the smear-out effect by the applied regression method. The upper-layer cooling is mainly due to radiative cooling. Strong mid–upper-level heating occurs at the time of the peak convection. The elevated warm anomalies and heating in this region produces eddy available potential energy, which acts to maintain the MJO activity against mechanical and thermal damping (Benedict and Randall 2007; Fu and Wang 2009). Figure 11 shows the decomposition of the Q1 field in this RAS scheme into dry static energy tendency, horizontal, and vertical dry static energy advection terms. As seen in the figure, the heat source (Q1) is mainly due to the vertical advection term (Fig. 11d). The tendency and horizontal advection terms appear one order of magnitude smaller than the Q1 and vertical advection contribution. In the plot of apparent moisture sink (Fig. 10f), strong moisture consumption (Q2) takes place on day 0 with the peak at the level of maximum specific moisture anomalies (i.e., 500–600 hPa). The nearly similar Q2 value compared to Q1 implies that apparent diabatic heating is mostly due to condensational latent heating. The general structure

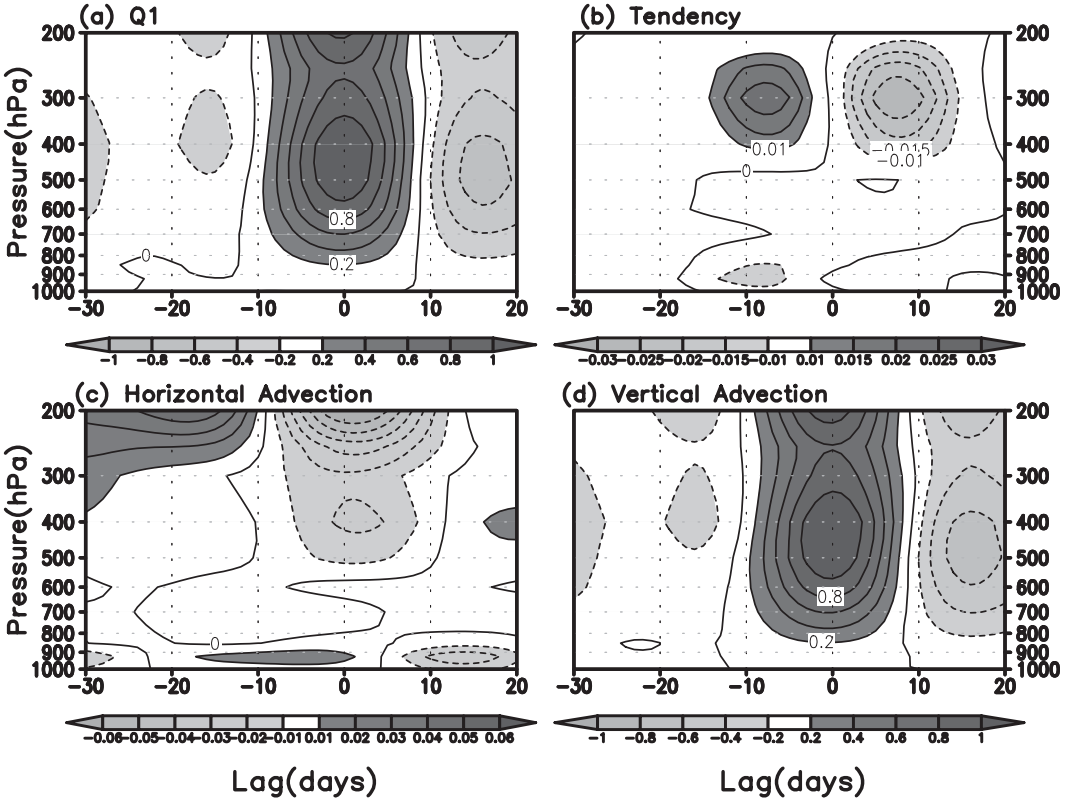

FIG. 11. The partition of (a) the Q1 fields into (b) dry static energy tendency, (c) horizontal dry static energy advection, and (d) vertical dry static energy advection terms in CFS T126RAS. Units are K day^{-1}.

in Q1 and Q2 is very similar to the observations of Benedict and Randall (2007, see their Fig. 6) and even, about 12%–15% difference between the peak values of Q1 and Q2 in the model is seen in the observations as well.

However, CFS T126 (Fig. 9) shows more or less weaker dynamic and thermodynamic anomalies than the observations and CFS T126RAS. Some features exist that are similar to CFS T126RAS and observations—premoistening and warm anomalies at the surface ~(15–10) days prior to the strongest convection (Figs. 9c,d)—but they are rather weak. Between days −20 and −10, in CFS T126 (Fig. 9d) the temperature anomalies in the whole troposphere is rather small and there is no cooler air in the upper troposphere, whereas in CFS T126RAS (Fig. 10d) the warm anomalies exist in the lower and middle troposphere and anomalously cool air appears in the upper troposphere, thereby forming a more unstable atmosphere. Diabatic heating (Fig. 9e) is also weak with its peak at 200 hPa and condensational moisture consumption (Fig. 9f) by precipitation in the troposphere is weaker. This is why CFS T126 appears to generate some of the main MJO characteristics, but it is not as strongly sustained as CFS T126RAS, so that the propagation across the Maritime Continent is not robust, although the remnant signal of convection and upper- and lower-level zonal wind anomalies exists over the western Pacific.

8) STRATIFORM HEATING

To more specifically pinpoint the reason why the RAS run produced better MJO simulation compared to the SAS run, we plot the vertical profiles of diabatic heating by its components (i.e., convective, stratiform, and radiative components) in Fig. 12. The vertical diffusion heating term is small so it is negligible. CFS T126 shows that the total diabatic heating is mainly from the deep convective heating, which is maximized at the levels of 400–500 hPa, but the stratiform heating (large-scale condensational heating) is very small. However, CFS T126RAS shows that both the convective heating and stratiform heating contribute to the total diabatic heating. The total heating in CFS T126RAS is ~1.5 times greater than that of the SAS run owing to the additional heating from the stratiform component. The heating profile of the stratiform component is canonical in that heating appears in the upper and middle troposphere above a melting layer (200–600 hPa) and cooling in the lower troposphere (below ~600 hPa; see Lin et al. 2004;

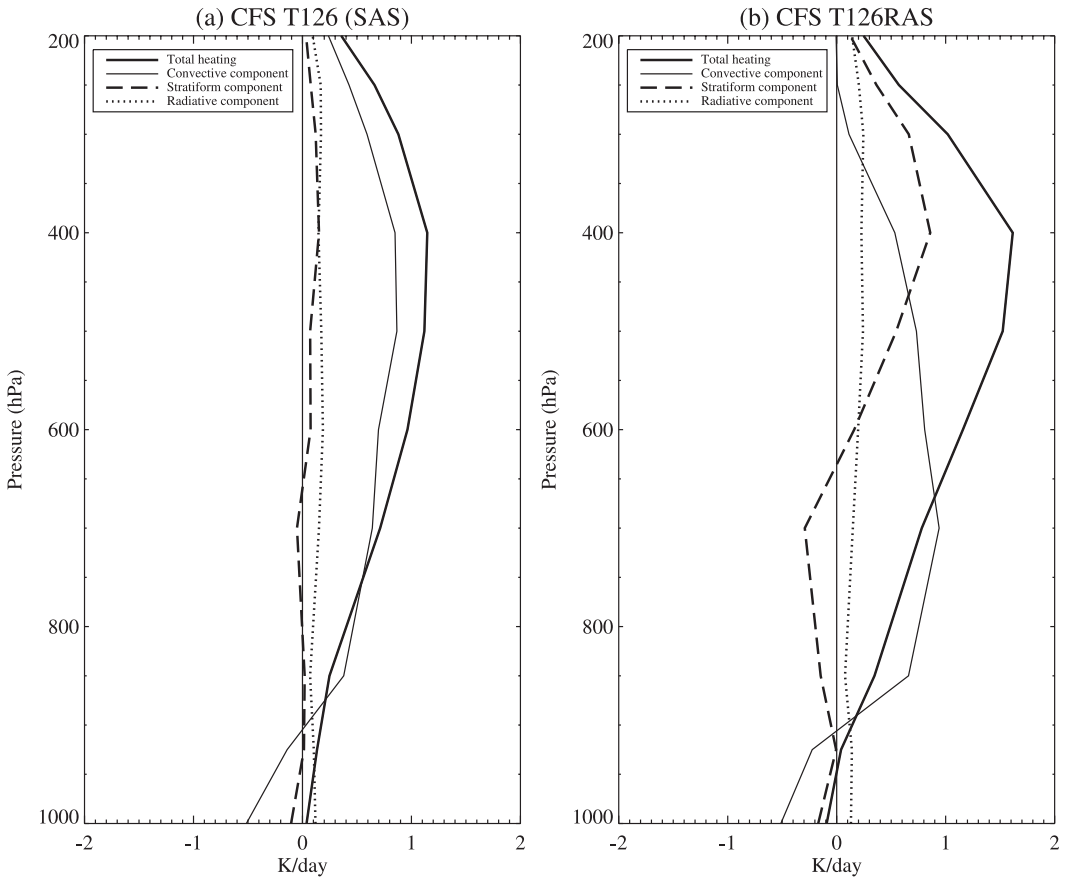

FIG. 12. The partition of the total vertical heating profile (thick solid line) into the convective component (thin solid line), the stratiform component (dashed line), and the radiative component (dotted line) for (a) CFS T126 and (b) CFS T126RAS.

Schumacher and Houze 2003; Fu and Wang 2009). The heating rate in the upper layer is 0.6 K day^{-1}, greater than the convective component and twice the cooling rate in the lower layer. This second-mode profile tends to significantly enhance the top heaviness of the total heating profile (Mapes 2000). The radiative heating (shortwave plus longwave radiative heating) is less than 20% of the convective heating. The convective heating center of CFS T126RAS appears 700 hPa, similar to the observed (TRMM PR) MJO convective heating peak located at 3–4 km (Morita et al. 2006). However, the convective heating center of CFS T126 occurs too high (at 400–500 hPa), presumably because the SAS scheme only considers one deepest cumulus cloud. From this wrong reason, CFS T126 exhibits a top-heavy heating profile to some degree.

The fraction of the stratiform rainfall to the total rainfall over the MJO development region is plotted in Fig. 13 for both runs. The stratiform rain fraction is greater than ~30% in CFS T126RAS, but that of the SAS run is around 10%. This result is consistent with the findings of Fu and Wang (2009), where a model-produced MJO is robustly sustained only when the model (ECHAM4) produces a significant proportion of stratiform rainfall (>30%), similar to the current study.

The observed link between deep cumulus ensembles and stratiform clouds in the tropics is through the supply of water vapor and cloud water detrained from cumulus updrafts to the environment and stratiform anvil clouds. Cooling of the environmental air by evaporation of detrained liquid water and moistening of the environment by evaporation of the detrained water and detrainment of the saturated air from cumulus clouds make the environment closer to a saturated state (and of course these, in turn, increase convective available potential energy for the deeper clouds); hence, the large-scale stratiform condensational heating appears in the upper and middle atmosphere. Again, the detrainment of the saturated air and the evaporation of detrained liquid water play a very important role in the development of cumulus convection and stratiform clouds by increasing the large-scale environment humidity. Under this humid

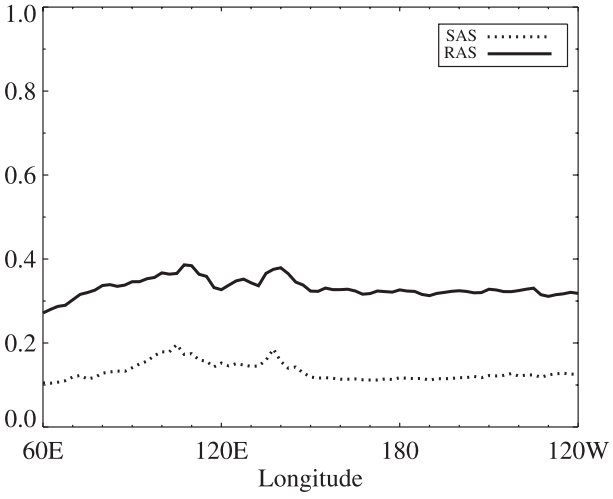

FIG. 13. The fraction of the stratiform rainfall to the total rainfall. The dotted line denotes CFS T126 and the solid line denotes CFS T126RAS.

environmental situation, more active convection develops and stronger convective updraft produces the more increased detrainment of water vapor and water condensate to the stratiform clouds, leading to an increased production of condensational heating in the middle to upper troposphere. This, in turn, generates the positive eddy available potential energy in the positive temperature anomaly region (see Fu and Wang 2009). This positive feedback between deep cumulus convection and stratiform clouds represents a moisture–stratiform instability theory proposed by Mapes (2000) and Kuang (2008). So, to check this process, the relative humidity fields are plotted using the OLR index (which is used in Figs. 9–12). Figure 14 shows the composite relative humidity fields as a function of lag days for CFS T126, CFS T126RAS, and their difference. The composite is formed only for the cases where the OLR index is less than −1.0 standard deviation. The two runs all show the gradual increase of relative humidity during earlier shallow convection and later deep convection periods, as well as the maximum moistening at the point of heaviest convection, implying the existence of sensitivity to the environmental humidity (Derbyshire et al. 2004). This sensitivity is observed in the tropics and regarded necessary for the development of strong convective events (Benedict and Randall 2007; Thayer-Calder and Randall 2009). However, the RAS run shows more humid environment than the SAS run during the cycle. The relative humidity differences of 5%–10% appear between 350 and 650 hPa (Fig. 14c), which corresponds to the levels of stratiform heating. The higher humidity leads to the easier penetration of convective clouds through the entire column of the troposphere without significant dilution by

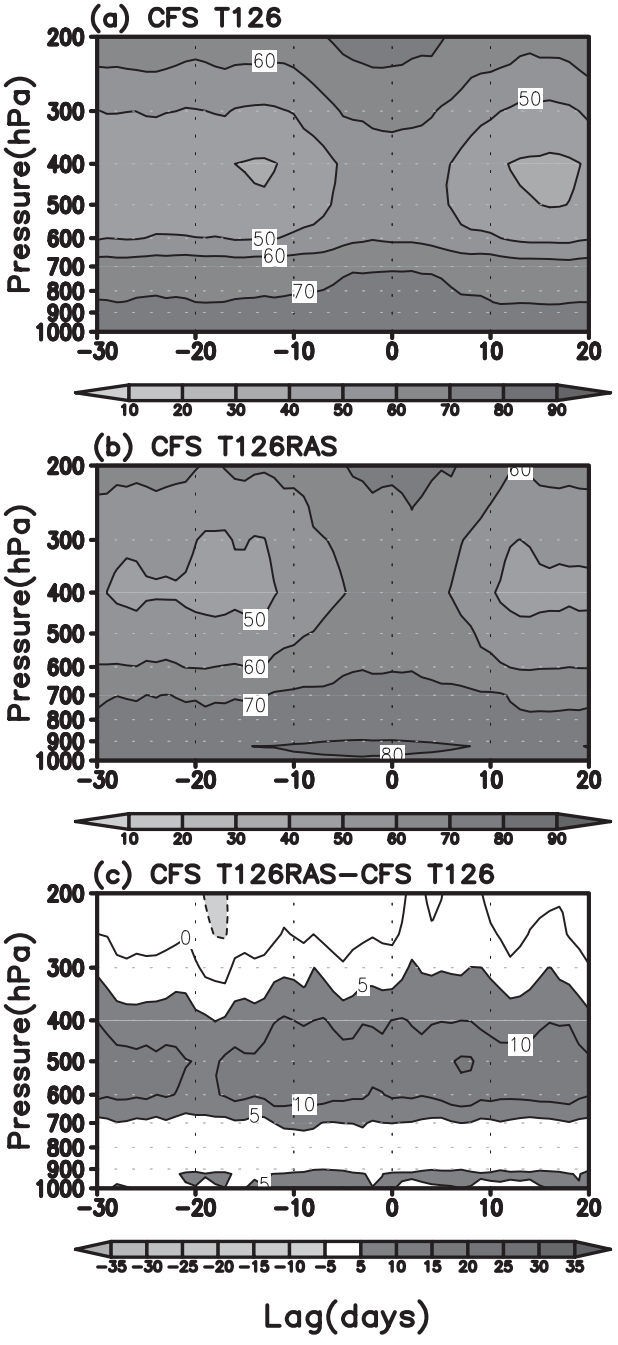

FIG. 14. The composite relative humidity (%) field as a function of lag days for (a) CFS T126, (b) CFS T126RAS, and (c) their difference (CFS T126RAS − CFS T126). The composite is formed only for the cases where the normalized OLR index (used in Fig. 9) is <-1.0 standard deviation (i.e., for the strong convection events).

entrainment of dry air. The RAS scheme considers cumulus ensembles with different cloud tops and so allows convective detrainment of moist air to the environment at the various levels (presumably as appeared in the Fig. 14c), enabling the increase of the relative humidity of the

environment in the middle–upper troposphere and the end result is stronger large-scale condensation and stratiform rainfall. Meanwhile, the SAS scheme considers one deep cloud with detrainment at cloud top only, leading to less moistening in the environment and subsequently reduced stratiform rainfall. That is, this difference results in the different detrainment of water vapor from convective clouds in the middle and upper troposphere and the different vertical heating profiles, which ultimately affects the development and propagation of the MJO.

9) LOWER-LEVEL MOISTURE CONVERGENCE

One of the prevailing mechanisms of the MJO is the frictional wave-CISK process. Kelvin and Rossby waves tend to form lower-level moisture convergence ahead of the MJO convection (Matthews 2000; Seo and Kim 2003, Hsu et al. 2004). To explicitly display the relationship between the MJO convection and lower-level moisture convergence in the coupled runs, the correlation coefficients presented in Fig. 4 are averaged over the Indian Ocean and the western Pacific regions (Fig. 15). In both regions, enhanced convection follows the moisture convergence with a ~(2–5-)day lag (Fig. 15a). CFS T126 shows a weak moisture convergence signal, which is about half of the observed convergence (Fig. 15b). The significantly weak moisture convergence in this area also appears in GFS T62 and CFS T62 (not shown). However, the CFS T126RAS run (Fig. 15c) has a stronger moisture convergence that leads the enhanced convection by ~(2–5) days, which is similar to the observations. The phasing and magnitude of the lower-level moisture convergence is a key factor for the development and propagation of the MJO and only the persistent interaction between the MJO convection and circulation waves ensures the MJO maintenance.

c. Global response to tropical heating of the MJO

It has been found that the MJO-related diabatic heating induces the circulation anomalies extending from the tropical region to the mid- and high latitudes (e.g., Matthews et al. 2004; Lin et al. 2006; and references therein). The teleconnection to the extratropics, especially over Asia, the North Pacific, North America, and the Atlantic, is formed via the Rossby wave train, and extratropical circulation anomalies impact rainfall events and surface air temperature in these areas (e.g., Higgins et al. 2000; Paegle et al. 2000; Jones and Schemm 2000; Jeong et al. 2005). Therefore, here we assess the capability of the improved MJO simulation to improve the simulation of extratropical circulation anomalies. To examine the global circulation patterns induced by MJO convective forcing, OLR and 200-hPa streamfunction anomalies are regressed onto PC1 and PC2. To represent the circulation response to the strong enhanced or suppressed MJO convection events, the regression is performed with respect to a deviation of PC1 = 2 and PC2 = 2, as in Matthews (2000) and Matthews et al. (2004). The time evolution of the eastward-propagating MJO convective forcing and circulation is then calculated as follows:

$$\hat{\psi}(\alpha) = \hat{\psi}(\mathrm{PC1})\sin\alpha + \hat{\psi}(\mathrm{PC2})\cos\alpha, \qquad (1)$$

where $\hat{\psi}$(PC1) and $\hat{\psi}$(PC2) are the regressed OLR or streamfunction scaled to two standard deviations of normalized PC1 and PC2, respectively; and α is the phase angle of the MJO cycle. Assuming a 48-day period for the MJO life cycle, the phase intervals of 45° correspond to the 6-day intervals.

Figure 16 shows the regression maps of the observed wintertime (November–March) OLR and streamfunction anomalies at 6-day intervals. Only the first half of the MJO cycle is shown while the other half is identical but has a sign reversal. A statistical test is performed using the two-tailed Student's *t* test. To estimate the degree of freedom conservatively, a 20-day decorrelation time scale (a quarter cycle for longer events) is selected. The calculated critical correlation for the 95% confidence level is approximately 0.18 and only statistically significant streamfunction regions are plotted in the figure. MJO convection anomalies develop over the Indian Ocean, propagate to the east and decay near the date line. An anticyclonic (cyclonic) flow couplet off the equator is located to the west of or collocated with the enhanced (suppressed) convection anomalies, and the westerly (easterly) anomalies along the equator appear to the east of the enhanced (suppressed) convection. This is indicative of a Rossby–Kelvin wave response to the MJO heating (e.g., Matthews 2000; Seo and Kim 2003). Along with these eastward-propagating convection anomalies, the figure clearly shows that the circulation anomalies associated with the Rossby–Kelvin waves also propagate to the east. The well-known circulation or wave features can be seen in the figure. For example, at $t = 0$ and $t = 6$, a westward retraction of the east Asian jet appears along ~30°N and the Pacific–North American (PNA)-like wave pattern is formed. Over the eastern Pacific, the Rossby wave propagation to the Southern Hemisphere through the westerly duct (Hoskins and Ambrizzi 1993) is seen from $t = 0$ to $t = 12$. A weak wave train in the Southern Hemisphere emanates from the Indian Ocean through the east of the date line, as shown at $t = 0$ (Fig. 16a) and more clearly at $t = 6$ (Fig. 16b).

Figures 17 and 18 represent the corresponding circulation response to the intraseasonal tropical heating in

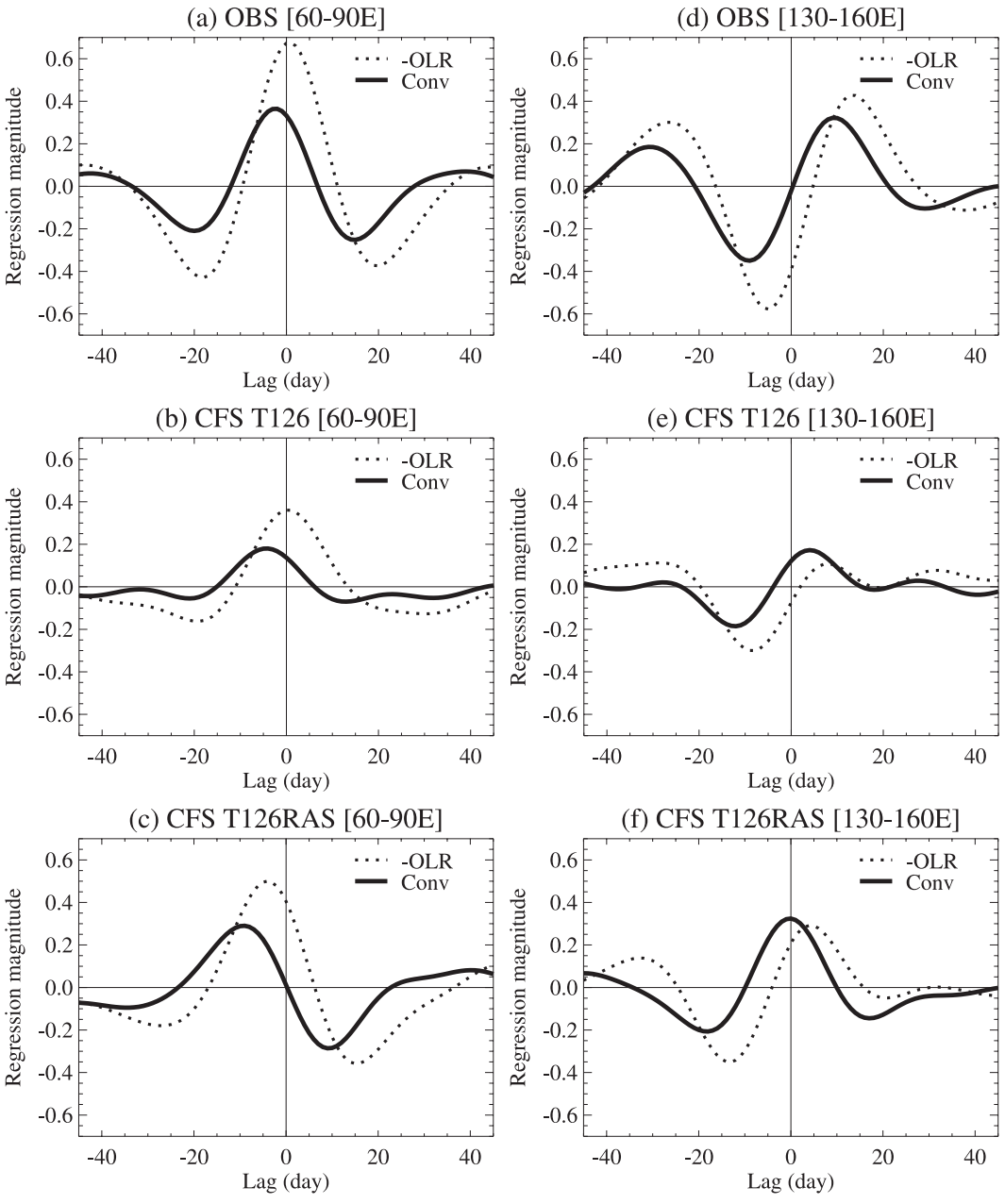

FIG. 15. Relationship between OLR and surface moisture convergence averaged over 10°S–10°N, 60°–90°E for (a) observations, (b) CFS T126, and (c) CFS T126RAS, and averaged over 10°S–10°N, 130°–160°E for (d) observations, (e) CFS T126, and (f) CFS T126RAS.

CFS T126 and CFS T126RAS. The convective anomalies in the CFS T126 simulation are much weaker than those in the observations, and thus the streamfunction anomalies are also weak. Since the convection anomalies diminish considerably and are broken up when they move across the Maritime Continent (i.e., Figs. 17a–c) so that no significant convection appears near the date line (i.e., no positive OLR anomalies over this area in Figs. 17b,c), the circulation anomalies coupled to the weakened convection are up to 2 times weaker than the observations. Meanwhile, CFS T126RAS (Fig. 18) successfully simulates the eastward propagation of the MJO convection. In fact, both the strength and size of the enhanced–suppressed convection anomalies are greater than the observed values throughout the cycle, producing the stronger circulation response. The overall structures of the streamfunction anomalies appear similar to the observations. The actual pattern correlation between the

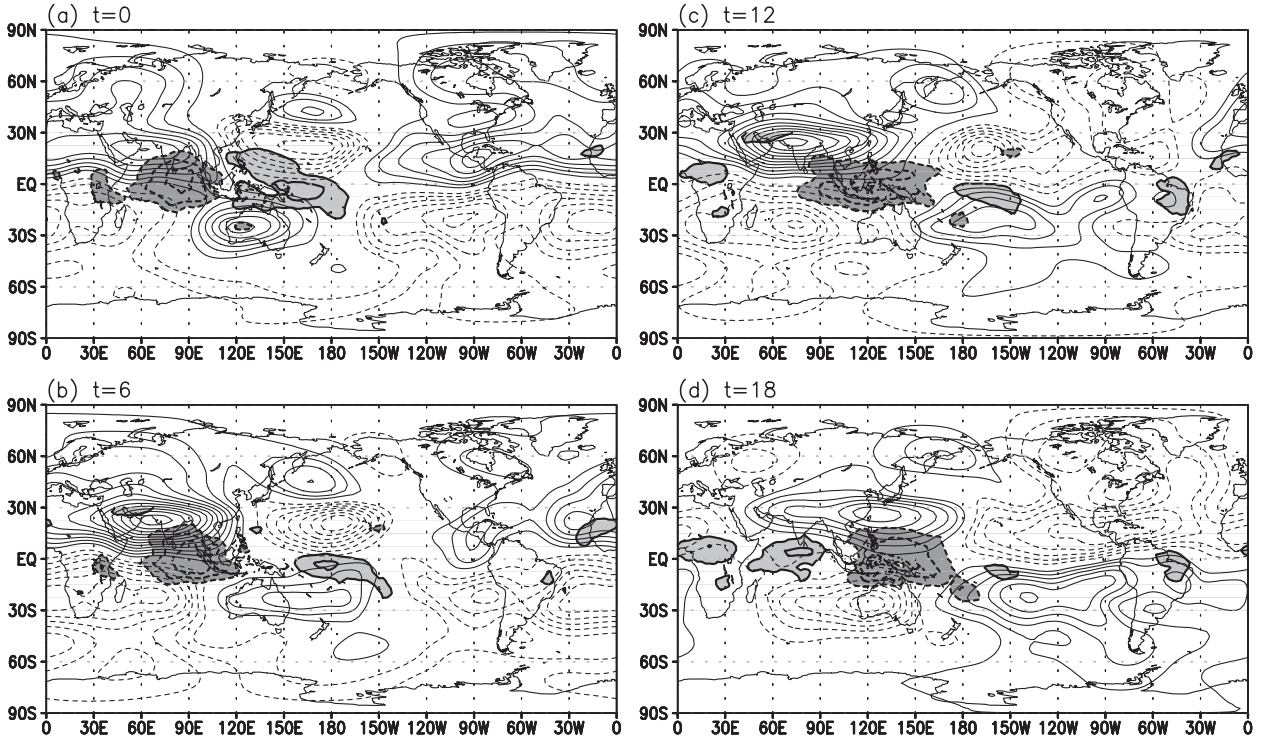

FIG. 16. Regression maps of observed wintertime OLR (shading) and 200-hPa streamfunction (contours) anomalies at 6-day intervals during the first half of the MJO cycle. The regressed magnitude is scaled to a deviation of PC1 = 2 and PC2 = 2. OLR is shaded heavily below -10 W m^{-2} and lightly above 10 W m^{-2}, with contour intervals of 10 W m^{-2}. The contour interval of the streamfunction is 1.4×10^6 m^2 s^{-1}. The 0 contour line is suppressed. The contoured streamfunction anomalies are approximately significant at the 95% confidence level.

regressed streamfunction in CFS T126RAS and the observation ranges from 0.84 to 0.91, which is much higher than the correlation of 0.47–0.78 between CFS T126 and observation. Again, CFS T126RAS simulates the PNA-like wave train, Rossby wave propagation in the eastern Pacific westerly duct, and wave propagation from the southern Indian Ocean to the downstream region. However, the suppressed convection over the western or central Pacific is shifted by ~30° to the east (Figs. 18a–c) compared to the observations, so the circulation response coupled to the shifted convection also appears 30° eastward. If the MJO convection over the Pacific is better simulated, the simulation of circulation and precipitation variations in the downstream region, including the Americas, will be much improved.

5. Summary and discussion

This study investigates the fidelity of simulating the tropical intraseasonal variability, with a focus on the MJO, in a series of atmosphere–ocean coupled and uncoupled long-term simulations using the NCEP models. The effect of air–sea coupling on the MJO is examined by comparing a 21-yr coupled simulation running from the fully coupled NCEP CFS model (CFS T62) and an AMIP simulation forced by the prescribed observed SST using the atmospheric GFS model (GFS T62). Another coupled simulation with a higher horizontal resolution model (CFS T126) is performed to investigate the impact of model horizontal resolution. These AMIP and coupled simulations are based on the SAS cumulus parameterization scheme. In order to examine the impact on the deep convection scheme, an additional coupled T126 run (CFS T126RAS) is conducted with the RAS scheme. The most dominant factors for the proper simulation of the MJO are deduced from these runs.

EOF and lagged regression analyses indicate that the interactive air–sea coupling greatly improves the coherence between convection, circulation and other surface fields. A higher horizontal resolution run (CFS T126) does not show any significant improvements in the intensity and structure. In fact, GFS T62, CFS T62, and CFS T126 all yield weaker 30–60-day variances that are not statistically distinguishable from the background red noise spectrum. Their eastward propagation is stalled over the Maritime Continent and far western Pacific,

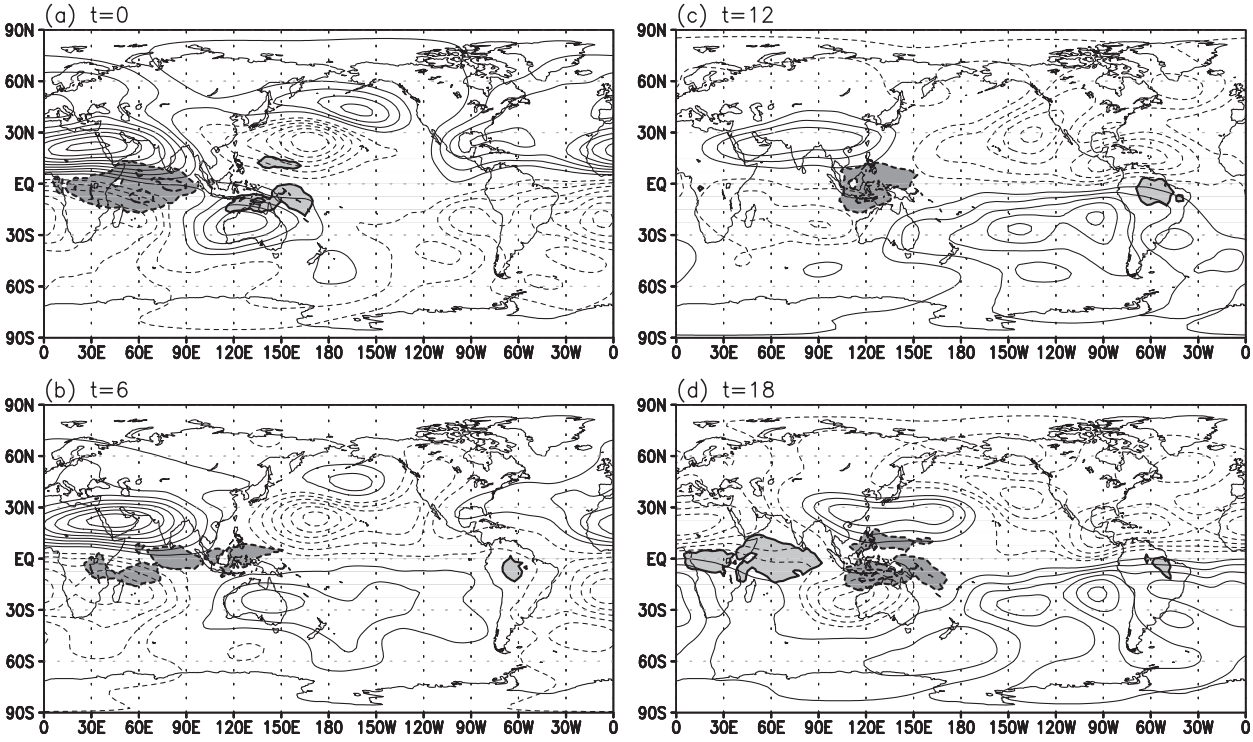

FIG. 17. As in Fig. 16, but for CFS T126.

which is similarly to that in many other climate models. In contrast to the model simulations using the SAS cumulus scheme, CFS T126RAS produces statistically significant spectral peaks in the MJO spectral band and the strength of MJO convection and circulation is greatly improved. Most of all, the ability of the MJO convection signal to penetrate into the Maritime Continent and western Pacific is demonstrated. Surface fluxes and the MJO convection show a similar lead–lag relationship to the observations. In particular, the surface moisture convergence signal in this model is comparable to the observation and propagates across the Maritime Continent region. The moisture convergence is located persistently to the east of the enhanced convection and induces the frictional convergence mechanism. However, the spectral analysis reveals that while the observed MJO has the strongest spectral power centered on zonal wavenumber 1, CFS T126RAS exhibits a richer zonal structure because of the presence of a convection signal over the Western Hemisphere. A careful examination of other climate models also reveals this behavior [see Lin et al. (2006); see also Seo et al. (2007) for boreal summer intraseasonal oscillation].

Furthermore, this study demonstrates that the improved MJO simulation in CFS T126RAS improves the simulation of global circulation anomalies. A preliminary result using a simple GFDL GCM and Rossby wave theory shows that the global circulation response is largely determined by the wintertime large-scale background mean flow and the location of the positive and negative heating anomalies in the MJO development region. Furthermore, nondivergent Rossby wave trains with zonal wavenumbers 2–4 largely make up the extratropical circulation anomalies, and the tropical circulation patterns (e.g., as shown in Fig. 16) are formed by the competition and amplification of the equatorially trapped westward-propagating Rossby wave and eastward-propagating Kelvin wave generated by MJO heating–cooling dipole. In addition, the magnitude of these circulation anomalies is almost linearly proportional to the strength of tropical diabatic forcing. Therefore, for the skillful prediction of weather and climate over Asia and North America as well as the tropical region, the improved simulation of tropical diabatic heating associated with the MJO is required.

Dominant factors in successfully simulating the basic features associated with the MJO have been discussed. A comparison of GFS 62 and CFS 62 shows the importance of interactive air–sea coupling. An increase in the resolution from T62 (which corresponds to ~2°) to T126 (~1°) in the coupled model does not improve the MJO simulation, but this may be achieved by future testing of a model resolution higher than T126. In addition, the simulated MJO in the NCEP models is not sensitive to basic-state vertical easterly wind shear and low-level

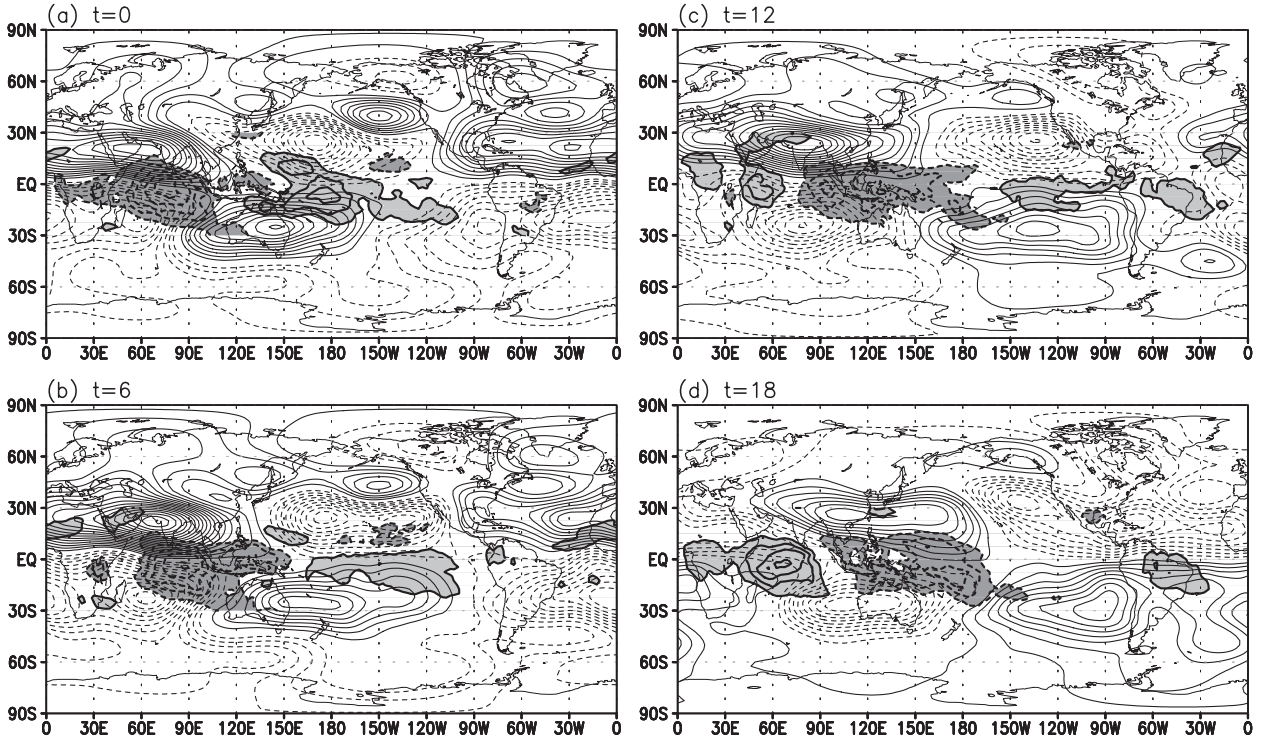

FIG. 18. As in Fig. 16, but for CFS T126RAS.

zonal winds in the tropics. CFS T126RAS continues to contain a vertical easterly wind shear one-third that of the observations and the 850-hPa easterly wind bias over the warm pools and Maritime Continent.

The cold SST bias over the eastern Indian Ocean weakens intraseasonal tropical convection. The evolution of CFS T62 convection for the winter season reveals that a convection anomaly develops over the central equatorial Indian Ocean and then splits into two entities (some hint of this can be seen in Fig. 17): one in the north and the other in the south of the equator. The northern one propagates northward and then decays at 10°N. Therefore, the CFS model tends to activate strong, unstable Rossby waves over the Indian Ocean because of this SST bias. This behavior was seen in the Hadley Centre coupled model (HadCM3) simulations (Inness and Slingo 2003). However, our study suggests that simulation of the eastward propagation across the Maritime Continent to the date line is not always guaranteed by the removal of a cold SST bias over the Indian Ocean and western Pacific. Even if a cold bias exists over the tropical western Pacific in CFS T126RAS, the eastward propagation across the Maritime Continent is reproduced. Therefore, the effect of the basic-state SST appears to be model dependent.

Surprisingly, the previous basic-model states in vertical wind shear, low-level zonal wind, precipitation, and SST appear to be insensitive for the proper MJO simulation. Rather, in this simulation, preconditioning of the atmosphere by shallow heating and moistening approximately 10–15 days prior to the subsequent intense MJO convection and a top-heavy vertical heating profile arising from convective detrainment of moisture to the environment and stratiform precipitation play a critical role in sustaining the MJO by generating eddy available potential energy. Again, this analysis stresses the importance of a moisture–stratiform instability process (Mapes 2000; Kuang 2008) for the proper simulation of the MJO. That is, the detrainment from convective plumes, on the one hand, moistens the grid-scale environment and induces the further development of the deep convective plumes. On the other hand, the detrained moisture produces and develops stratiform anvil clouds and so additional condensational heating in the upper and middle troposphere, forming a top-heavy heating profile and enhancing the instability. It is stratiform heating that is considered an essential element for this positive feedback process between moisture and convective–stratiform clouds.

In addition, the surface moisture convergence is persistently located to the east of the enhanced convection and induced the frictional wave-CISK mechanism. More active convective–stratiform cloud activity along the tropics in the CFS T126RAS model enhances lower-level circulation and moisture convergence to the east of

the enhanced convection, which in turn feeds back to the expansion of the MJO convective entities to the east. The persistent strong interaction between the convection–stratiform cloud process and large-scale circulation gives rise to the continued eastward propagation across the Maritime Continent. On the other hand, in CFS T126, the covariability between warm and diabatic heating anomalies in the middle and upper troposphere are smaller, so available potential energy, which acts to fuel the MJO convection, is weaker. Consequently, a numerical model should simulate the following three processes for the robust simulation of the MJO and these may serve as a baseline framework for other GCM simulations and forecasts: 1) a moisture–stratiform instability process (a top-heavy heating profile from sufficient stratiform heating and correct feedback process between moisture and convective–stratiform clouds); 2) the low-level moisture convergence to the east of MJO convection (through the appropriate moisture convective–stratiform cloud processes and circulation interactions); and 3) a discharge–recharge mechanism (Bladé and Hartmann 1993; wherein instability or moist static energy is accumulated and released before and after peak precipitation events, respectively) which is, in the model simulation, associated with a preconditioning of atmosphere for deep convection and an appropriate time scale for phase change). Note that both CFS T126 runs show an increased relative humidity at the time of maximum convection and therefore sensitivity of the environmental humidity to the development of convective plumes (Derbyshire et al. 2004) does not always guarantee the successful simulation of the MJO. Rather, more complex constraints such as moisture cloud processes–large-scale circulation interactions, as presented above, should be examined in detail.

There are some deficiencies of the simulation with the RAS scheme. Most of all, the amplitude of the MJO is stronger than the observed and extends farther into the east Pacific. A space–time spectral analysis (not shown) implies that this is mainly due to excessive activity in the higher zonal wavenumber than the characteristic zonal scale of the MJO. The excessive variability might be related to the positive feedback mechanism characterized by the successive processes of enhanced moistening by detrainment, enhanced stratiform heating, increased atmospheric instability, and more convection and detrainment. This portion of variability is not considered to be dynamically coherent. This study contains several limitations also. The most important one is that we are unable to determine specifically which elements or parameters of the RAS scheme are most effective for producing the improved MJO simulation. For instance, it is impossible to determine which components [e.g., shallow convection, entrainment–detrainment rate, downdraft, environmental humidity, interaction with boundary layer process (e.g., entrainment at the boundary layer top), mass-flux closure and partitioning and stratiform heating] are responsible for the reduced autocorrelation seen in CFS T126RAS (see Lin et al. 2006). A carefully designed sensitivity test will be required to resolve these issues.

Acknowledgments. The authors would like to thank Dr. Jialin Lin at Ohio State University, Dr. S. Moothi at EMC/NCEP/NOAA, and the anonymous reviewers for their helpful and constructive comments and suggestions. This work was funded by the Korea Meteorological Administration Research and Development Program under Grant CATER 2007-4208. This work was supported by the Korea Institute of Science and Technology Information.

REFERENCES

Arakawa, A., and W. H. Schubert, 1974: Interaction of cumulus cloud ensemble with the large-scale environment. Part I. *J. Atmos. Sci.,* **31,** 674–701.

Benedict, J. J., and D. A. Randall, 2007: Observed characteristics of the MJO relative to maximum rainfall. *J. Atmos. Sci.,* **64,** 2332–2354.

Bladé, I., and D. L. Hartmann, 1993: Tropical intraseasonal oscillations in a simple nonlinear model. *J. Atmos. Sci.,* **50,** 2922–2939.

Boyle, J., S. Klein, G. Zhang, S. Xie, and X. Wei, 2008: Climate model forecast experiments for TOGA COARE. *Mon. Wea. Rev.,* **136,** 808–832.

Das, S., A. K. Mitra, G. R. Ivengar, and J. Singh, 2002: Skill of medium-range foreasts over the Indian monsoon region using different parameterizations for deep convection. *Wea. Forecasting,* **17,** 1194–1210.

Derbyshire, S. H., I. Beau, P. Bechtold, J.-Y. Grandpeix, J.-M. Piriou, J.-L. Redelsperger, and P. M. M. Soares, 2004: Sensitivity of moist convection to environmental humidity. *Quart. J. Roy. Meteor. Soc.,* **130,** 3055–3079.

Duchon, C. E., 1979: Lanczos filtering in one and two dimensions. *J. Appl. Meteor.,* **18,** 1016–1022.

Flatau, M., P. J. Flatau, P. Phoebus, and P. P. Niiler, 1997: The feedback between equatorial convection and local radiative and evaporative process: The implication for intraseasonal oscillations. *J. Atmos. Sci.,* **54,** 2373–2386.

Fu, X., and B. Wang, 2009: Critical roles of the stratiform rainfall in sustaining the Madden–Julian oscillation: GCM experiments. *J. Climate,* **22,** 3939–3959.

——, B. Yang, G. Bao, and B. Wang, 2008: Sea surface temperature feedback extends the predictability of tropical intraseasonal oscillation. *Mon. Wea. Rev.,* **136,** 577–597.

Grell, G. A., 1993: Prognostic evaluation of assumptions used by cumulus parameterization. *Mon. Wea. Rev.,* **121,** 764–787.

Hendon, H. H., 2000: Impact of air–sea coupling on the Madden–Julian oscillation in a general circulation model. *J. Atmos. Sci.,* **57,** 3939–3952.

Higgins, R. W., J.-K. E. Schemm, W. Shi, and A. Leetmaa, 2000: Extreme precipitation events in the western United State related to tropical forcing. *J. Climate,* **13,** 793–820.

Hoskins, B. J., and T. Ambrizzi, 1993: Rossby wave propagation on a realistic longitudinally varying flow. *J. Atmos. Sci.,* **50,** 1661–1671.

Hsu, H.-H., C.-H. Weng, and C.-H. Wu, 2004: Contrasting characteristics between the northward and eastward propagation of the intraseasonal oscillation during the boreal summer. *J. Climate,* **17,** 727–743.

Inness, P. M., and J. M. Slingo, 2003: Simulation of the Madden–Julian oscillation in a coupled general circulation model. Part II: The role of the basic state. *J. Climate,* **16,** 365–382.

——, and ——, 2006: The interaction of the Madden–Julian oscillation with the maritime continent in a GCM. *Quart. J. Roy. Meteor. Soc.,* **132,** 1645–1667.

——, ——, S. J. Woolnough, R. B. Neale, and V. D. Rope, 2001: Organization of tropical convection in a GCM with varying vertical resolution: Implications for the simulation of the Madden–Julian oscillation. *Climate Dyn.,* **17,** 777–793.

——, ——, E. Guilyardi, and J. Cole, 2003: Simulation of the Madden–Julian oscillation in a coupled general circulation model. Part I: Comparisons with observations and an atmosphere-only GCM. *J. Climate,* **16,** 345–364.

Jeong, J.-H., C.-H. Ho, B.-M. Kim, and W.-T. Kwon, 2005: Influence of the Madden–Julian Oscillation on wintertime surface air temperature and cold surges in east Asia. *J. Geophys. Res.,* **110,** D11104, doi:10.1029/2004JD005408.

Jones, C., and J.-K. E. Schemm, 2000: The influence of intraseasonal variations on medium-range weather forecasts over South America. *Mon. Wea. Rev.,* **128,** 486–494.

Kanamitsu, M., W. Ebisuzaki, J. Woollen, S.-K. Yang, J. J. Hnilo, M. Fiorino, and G. L. Potter, 2002: NCEP-DOE AMIP-II Reanalysis (R-2). *Bull. Amer. Meteor. Soc.,* **83,** 1631–1643.

Kim, D., and Coauthors, 2009a: Application of MJO simulation diagnostics to climate models. *J. Climate,* **22,** 6413–6436.

Kim, H.-M., C. D. Hoyos, P. J. Webster, and I.-S. Kang, 2009b: Ocean–atmosphere coupling and the boreal winter MJO. *Climate Dyn.,* in press, doi:10.1007/s00382-009-0612-x.

Krishnamurti, T. N., D. K. Osterhof, and A. V. Mehta, 1988: Air-sea interaction on the time scale of 30 to 50 days. *J. Atmos. Sci.,* **45,** 1304–1322.

Kuang, Z. M., 2008: A moisture-stratiform instability for convectively coupled waves. *J. Atmos. Sci.,* **65,** 834–854.

Liebmann, B., and C. A. Smith, 1996: Description of a complete (interpolated) outgoing longwave radiation dataset. *Bull. Amer. Meteor. Soc.,* **77,** 1275–1277.

Lin, J.-L., 2007: The double-ITCZ problem in IPCC AR4 coupled GCMs: Ocean–atmosphere feedback analysis. *J. Climate,* **20,** 4497–4525.

——, B. Mapes, M. Zhang, and M. Newman, 2004: Stratiform precipitation, vertical heating profiles, and the Madden–Julian oscillation. *J. Atmos. Sci.,* **61,** 296–309.

——, and Coauthors, 2006: Tropical intraseasonal variability in 14 IPCC AR4 climate models. Part I: Convective signals. *J. Climate,* **19,** 2665–2690.

Maloney, E. D., and D. L. Hartmann, 1998: Frictional moisture convergence in a composite life cycle of the Madden–Julian oscillation. *J. Climate,* **11,** 2387–2403.

Mapes, B. E., 2000: Convective inhibition, subgrid-scale triggering energy, and stratiform instability in a toy tropical wave model. *J. Atmos. Sci.,* **57,** 1515–1535.

Matthews, A. J., 2000: Propagation mechanisms for Madden–Julian oscillation. *Quart. J. Roy. Meteor. Soc.,* **126,** 2637–2651.

——, B. J. Hoskins, and M. Masutani, 2004: The global response to tropical heating in the Madden–Julian oscillation during the northern winter. *Quart. J. Roy. Meteor. Soc.,* **130,** 1911–2011.

Moorthi, S., and M. J. Suarez, 1992: Relaxed Arakawa–Schubert: A parameterization of moist convection for general circulation models. *Mon. Wea. Rev.,* **120,** 978–1002.

——, and ——, 1999: Documentation of version 2 of relaxed Arakawa–Schubert cumulus parameterization with convective downdrafts. NOAA Office Note 99-01, 44 pp.

Morita, J., Y. Takayabu, and S. Shige, 2006: Analysis of rainfall characteristics of the Madden–Julian oscillation using TRMM satellite data. *Dyn. Atmos. Oceans,* **42,** 107–126.

Pacanowski, R. C., and S. M. Griffies, 1998: MOM 3.0 manual. NOAA/Geophysical Fluid Dynamics Laboratory, Princeton, NJ, 668 pp.

Paegle, J. N., L. A. Byerke, and K. C. Mo, 2000: Intraseasonal modulation of South American summer precipitation. *Mon. Wea. Rev.,* **128,** 837–850.

Pan, H.-L., and W.-S. Wu, 1995: Implementing a mass flux convection parameterization package for the NMC medium-range forecast model. NMC Office Note 409, 39 pp.

Reynolds, R. W., N. A. Rayner, T. M. Smith, D. C. Stokes, and W. Wang, 2002: An improved in situ and satellite SST analysis for climate. *J. Climate,* **15,** 1609–1625.

Saha, S., and Coauthors, 2006: The NCEP Climate Forecast System. *J. Climate,* **19,** 3483–3517.

Salby, M. L., R. R. Garcia, and H. H. Hendon, 1994: Planetary-scale circulations in the presence of climatological and wave-induced heating. *J. Atmos. Sci.,* **51,** 2344–2367.

Schumacher, C., and R. A. Houze Jr., 2003: Stratiform rain in the tropics as seen by the TRMM precipitation radar. *J. Climate,* **16,** 1739–1756.

Seo, K.-H., and K.-Y. Kim, 2003: Propagation and initiation mechanisms of the Madden–Julian oscillation. *J. Geophys. Res.,* **108,** 4384–4405.

——, and Y. Xue, 2005: MJO-related oceanic Kelvin waves and the ENSO cycle: A study with the NCEP Global Ocean Data Assimilation. *Geophys. Res. Lett.,* **32,** L07712, doi:10.1029/2005GL022511.

——, J.-K. Schemm, C. Jones, and S. Moorthi, 2005: Forecast skill of the tropical intraseasonal oscillation in the NCEP GFS dynamical extended range forecasts. *Climate Dyn.,* **25,** 265–284.

——, J.-K. E. Schemm, W. Wang, and A. Kumar, 2007: The boreal summer intraseasonal oscillation simulated in the NCEP Climate Forecast System (CFS): The effect of sea surface temperature. *Mon. Wea. Rev.,* **135,** 1807–1827.

——, W. Wang, J. Gottschalck, Q. Zhang, J.-K. E. Schemm, W. R. Higgins, and A. Kumar, 2009: Evaluation of MJO forecast skill from several statistical and dynamical forecast models. *J. Climate,* **22,** 2372–2388.

Slingo, J. M., and Coauthors, 1996: Intraseasonal oscillations in 15 atmospheric general circulation models: Results from an AMIP diagnostic subproject. *Climate Dyn.,* **12,** 325–357.

Sperber, K. R., S. Gualdi, S. Legutke, and V. Gayler, 2005: The Madden–Julian oscillation in ECHAM4 coupled and uncoupled general circulation models. *Climate Dyn.,* **25,** 117–140.

Thayer-Calder, K., and D. A. Randall, 2009: The role of convective moistening in the Madden–Julian oscillation. *J. Atmos. Sci.,* **66,** 3297–3312.

Tokioka, T., K. Yamazaki, A. Kitoh, and T. Ose, 1988: The equatorial 30-60-day oscillation and the Arakawa-Schubert penetrative cumulus parameterization. *J. Meteor. Soc. Japan,* **66,** 883–901.

Waliser, D. E., K. E. Lau, and J. H. Kim, 1999: The influence of coupled sea surface temperatures on the Madden–Julian

oscillation: A model perturbation experiment. *J. Atmos. Sci.,* **56,** 333–358.

Wang, B., 1988: Dynamics of tropical low-frequency waves: An analysis of the moist Kelvin wave. *J. Atmos. Sci.,* **45,** 2051–2065.

Wang, W., and M. E. Schlesinger, 1999: The dependence on convection parameterization of the tropical intraseasonal oscillation simulated by the UIUC 11-layer atmospheric GCM. *J. Climate,* **12,** 1423–1457.

——, S. Saha, H.-L. Pan, S. Nadiga, and G. White, 2005: Simulation of ENSO in the new NCEP Coupled Forecast System Model (CFS). *Mon. Wea. Rev.,* **133,** 1574–1593.

Wheeler, M., and H. H. Hendon, 2004: An all-season real-time multivariate MJO index: Development of an index for monitoring and prediction. *Mon. Wea. Rev.,* **132,** 1917–1932.

Woolnough, S. J., J. M. Slingo, and B. J. Hoskins, 2000: The relationship between convection and sea surface temperature on intraseasonal timescales. *J. Climate,* **13,** 2086–2104.

Xie, P., and P. A. Arkin, 1997: Global precipitation: A 17-year monthly analysis based on gauge observations, satellite estimates, and numerical model outputs. *Bull. Amer. Meteor. Soc.,* **78,** 2539–2558.

Yanai, M., S. Esbensen, and J.-H. Chu, 1973: Determination of bulk properties of tropical cloud clusters from large-scale heat and moisture budgets. *J. Atmos. Sci.,* **30,** 611–627.

Zhang, C., 1996: Atmospheric intraseasonal variability at the surface in the tropical western Pacific Ocean. *J. Atmos. Sci.,* **53,** 739–758.

Zhang, G., and M. Mu, 2005: Simulation of the Madden–Julian oscillation in the NCAR CCM3 using a revised Zhang–McFarlane convection parameterization scheme. *J. Climate,* **18,** 4046–4064.

Zhang, M. H., and M. A. Geller, 1994: Selective excitation of tropical atmospheric waves in wave-CISK: Effect of vertical wind shear. *J. Atmos. Sci.,* **51,** 353–368.

Zhu, H., H. Hendon, and C. Jakob, 2009: Convection in a parameterized and superparameterized model and its role in the representation of the MJO. *J. Atmos. Sci.,* **66,** 2796–2811.